energies

MDPI

Article

Integrating Computational and Experimental Methods for Thermal Energy Storage: A Predictive Artificial Neural Network Model for Cold and Hot Sensible Systems

Antonio Rosato [1,*], Mohammad El Youssef [1], Antonio Ciervo [1], Hussein Daoud [2], Ahmed Al-Salaymeh [2,3] and Mohamed G. Ghorab [4]

[1] Department of Architecture and Industrial Design, University of Campania Luigi Vanvitelli, via San Lorenzo 4, 81031 Aversa, Italy; mohammad.elyoussef@unicampania.it (M.E.Y.); antonio.ciervo@unicampania.it (A.C.)
[2] Mechanical Engineering Department, National University College of Technology, Amman 11592, Jordan; h.daoud@nuct.edu.jo (H.D.); salaymeh@ju.edu.jo (A.A.-S.)
[3] Mechanical Engineering Department, School of Engineering, The University of Jordan, Amman 11942, Jordan
[4] Department of Mechanical Engineering, Alexandria University, Alexandria 21544, Egypt
* Correspondence: antonio.rosato@unicampania.it

Abstract

This study introduces a predictive model based on artificial neural networks (ANNs) for estimating the dynamic performance of commercially available sensible thermal energy storage (STES) systems. The model was trained and validated using high-resolution experimental data measured from two vertical cylindrical tanks (0.3 m^3 each) including internal heat exchangers and operating under both heating and cooling modes. A comprehensive sensitivity analysis was conducted on 28 ANN architectures by varying the number of hidden neurons and input delays. The optimal configuration, designated as ANN5 (12 neurons, delay = 1), demonstrated superior accuracy in predicting temperature profiles and energy exchange. Validation against an independent dataset confirmed the model's robustness, achieving normalized root mean square errors (NRMSEs) between 0.0022 and 0.0061 for the hot tank and between 0.0057 and 0.0283 for the cold tank. Energy prediction errors were within −3.87% for charging and 0.09% for discharging in heating mode, and 7.08% for charging and 0.13% discharging in cooling mode, respectively. These results highlight the potential of ANN-based approaches for real-time control, forecasting, and digital twin applications in STES systems.

Keywords: sensible thermal energy storage; thermal stratification; predictive model; experimental field performance; artificial neural network; energy system simulation

Check for updates

Academic Editor: Ioan Sarbu

Received: 11 December 2025
Revised: 19 January 2026
Accepted: 23 January 2026
Published: 28 January 2026

Copyright: © 2026 by the authors. Licensee MDPI, Basel, Switzerland. This article is an open access article distributed under the terms and conditions of the Creative Commons Attribution (CC BY) license.

1. Introduction

Thermal energy storage (TES) systems are essential for decoupling energy generation from consumption, enabling short-term storage of thermal energy at low or high temperatures for later use. These systems improve energy efficiency by storing surplus energy during off-peak periods and releasing it during peak demand, thereby reducing operational costs and enhancing system reliability. This capability is particularly critical for integrating intermittent renewable sources, such as solar energy, into smart low-carbon buildings [1]. TES technologies are generally classified into three categories: sensible, latent, and thermochemical storage. Among these, sensible thermal energy storage (STES) is the most widely adopted due to its simplicity, cost-effectiveness, and environmental

compatibility [2,3]. STES systems store energy by varying the temperature of a storage medium without inducing a phase change, making them easier to control and maintain compared to latent or chemical alternatives. In recent decades, STES has gained significant attention for its role in solar energy utilization, renewable integration, and greenhouse gas mitigation [4–6]. Moreover, investigating and understanding STES behavior under transient conditions is very important as it significantly influences the performance of the energy systems in which they are used [7]. According to Elsheikh et al. [8] and Ji et al. [9], experimental investigations are crucial for validating the performance of energy systems, but they are inherently limited by the significant time and resource expenditure required to conduct an adequate number of tests. Furthermore, empirical findings are often constrained by a limited set of boundary conditions and parameter ranges, thereby restricting their general applicability. These limitations underscore the necessity of employing robust and detailed simulation models. ASHRAE Handbook [10] recognizes two different main approaches in developing simulation models of energy systems: the forward approach and the data-driven approach. The objective of forward approach models is to use known model structures and parameters to predict the model outputs under specified inputs. On the other hand, the objective of data-driven methods is to derive a mathematical description of a system and estimate its parameters by leveraging empirical data from its measured inputs and outputs. The forward approach for STESs depends on complex differential equations that govern the behavior of the storage medium [11,12]; related models use simplifications, and approximation methods are often applied; the determination of system parameters (such as the heat conduction and convection coefficients) for these models sometimes needs complicated measurements [11]. The data-driven approaches are classified into two primary groups [9]: the black-box approach and the gray-box approach. The black-box approach involves creating a regression model, either simple or multivariate, to directly correlate the system's outputs to its input parameters. Conversely, the gray-box approach first formulates a physical model to represent the system's physical configuration and subsequently uses statistical analysis to identify and estimate its important parameters. Unlike gray-box models, black-box models do not require a very detailed knowledge of the system's physical characteristics or explicit parameter measurements; they learn the relationships between the model inputs and outputs by analyzing previously recorded performance data [13]; this makes the black-box approach simpler, less computationally intensive, and more accurate than the gray-box approach, particularly for systems exhibiting highly dynamic behavior or complex processes [11].

Artificial neural networks (ANNs) have emerged as a powerful tool. Inspired by biological neural systems, ANNs can capture nonlinear relationships and dynamic interactions between system inputs and outputs [13]. Their ability to generalize from historical data makes them well-suited for predicting STES system performance under diverse operating conditions. Each network consists of one input layer, one or more hidden layers, and one output layer. Each hidden layer consists of a number of neurons, with each neuron connected with the neurons of the previous and the next layers via connections called synapses. Each synapse has a weight which is multiplied by its own input; all the weighted inputs are then summed in addition to an external bias; then, an activation function is applied to this summation. ANNs are trained based on input data to predict one or more outputs; this happens by comparing the predicted outputs with the target outputs and modifying the weights and the biases accordingly via an iterative process. The iterations (which are called epochs) continue until the difference between the predicted and target outputs reaches a predefined value or after a predefined number of epochs; in addition, randomly selected data points are used for validation in order to prevent overfitting and maintain the network generalization (avoiding it to become specific for the data used

during the training process). Analytical models rely on simplified assumptions that limit accuracy when applied to realistic systems involving nonlinear thermal behavior and transient operating conditions [14,15]. Computational fluid dynamics (CFD) models provide high-fidelity predictions, but require extensive computational resources, detailed geometrical information, and complex meshing, making them impractical for resolving transient heat transfer and fluid dynamics within TESs [14,15]. In contrast, the proposed ANN model overcomes these limitations by learning the complex thermal interactions directly from data, providing accurate predictions without restrictive assumptions; it provides rapid predictions once trained, requiring only a small set of measurable weather and operating parameters as inputs [14,15].

According to Sioshansi et al. [16], STES systems face several unresolved modeling challenges. First, accurately representing the physical behavior of STES systems is difficult, as efficiency and heat losses vary over time and are often oversimplified in simulation models. Second, the modeling process can be computationally demanding due to the interactions between system components and boundary conditions. Third, realistic representation of operational constraints is necessary to ensure that the model reflects actual system performance. On the other hand, ANNs have emerged as promising and innovative tools for addressing these challenges, as they can reduce computational time and provide high accuracy and reliability in predicting the performance of complex energy systems [12]. The application of ANNs for modeling energy systems has garnered substantial research interest. Elsheikh et al. [8], Kalogirou [13], and Ji et al. [9] highlighted dozens of scientific works that adopted ANNs in solar, heating, ventilation, air-conditioning, and power-generation systems, as well as load-forecasting applications.

1.1. ANN-Based Models of STESs: Literature Review

A substantial body of research has been conducted with the objective of developing ANN-based models for STESs. Amarasinghe et al. [17] presented a control framework based on ANNs to control the operation of a water STES with the aim of optimizing the usage of thermal energy stored and, therefore, reducing energy costs. Lee et al. [18] developed two separate ANN-based networks to model a chilled water STES as well as a borehole heat exchanger. In particular, the data required by the ANN-based network for the STES were derived by using a physics-based multi-node model; they used a total of 960,000 data points (70% of these data points were used for training, 15% for validation, and 15% for testing the ANNs). The temperatures at the top and bottom of the STES were considered as target outputs of the ANN-based network. The ANN-based model for the STES was developed via the MATLAB platform [19] using the feed-forward network with the Levenberg–Marquardt algorithm as the training function, the sigmoid function as the activation function for hidden layers, and the linear function as the activation function for the output layer. They optimized the ANN-based network by considering multiple combinations of different model inputs, hidden layers, and neurons in each layer. The best results were achieved in the case of a ANN architecture consisting of 22 inputs, 2 hidden layers, and 30 neurons per each hidden layer, which yielded a coefficient of determination equal to 0.999 and a root mean square error equal to 0.0204 °C while comparing predicted and target values. Siahoui et al. [20] studied the thermal performance of an underground vertical cylindrical cold-water STES via both an analytical approach and an ANN-based model. Both the diameter and the height of the storage were equal to 12 m. The multilayer feed-forward network training was adopted as the back propagation algorithm for the ANN. The tangent sigmoid function was adopted as the transfer function in the hidden layer, while the linear function was considered as the transfer function in the output layer. The desired outputs were the temperatures at specified levels of the tank.

Siahoui et al. [20] investigated various training functions to optimize their ANN-based model. Their results showed that the minimum error was produced by a descent approach with a variable learning rate and momentum. Additionally, they performed an optimization of the network's hidden layer, establishing an optimal neurons number of 20. A good agreement was found between the experimental data and the results predicted by the ANN-based method. Diez et al. [21] developed an ANN-based model to predict the performance of a solar-heated water STES with no fluid flowing either into or out of the tank. The tank was a vertical cylinder with a capacity of 150 L, and it contained an internal heat exchanger connected with a solar collector. The tank was located inside a lab with almost constant ambient temperature around it. Temperatures were recorded at eight layers inside the tank with a time step of 10 min. The ANN-based model was expected to predict the future temperatures at the above-mentioned eight layers inside the tank starting from the corresponding temperatures measured at the previous time step used as inputs. The model was developed using the MATLAB neural network toolbox [19]; it consisted of 8 inputs and 8 outputs, with 16 neurons in the hidden layer, and the hyperbolic tangent sigmoid was adopted as the transfer function in the hidden layer and the linear function was used in the output layer. Géczy-Víg and Farkas [11] used ANNs to study the stratification inside a vertical water 0.15 m^3 STES used for domestic hot-water application. The STES was connected with a solar thermal collector through an internal heat exchanger. The authors collected the data with a sampling interval of 1 min during the period between July 5 and December 22 of 2006. An ANN-based model with eight neurons in the hidden layer was used to predict the water temperature corresponding to eight different layers inside the tank. The modeling was performed using the MATLAB neural network toolbox [19]. The Levenberg–Marquardt algorithm was adopted for training, and the tangent–sigmoid function was adopted as the transfer function. A set of 30,943 data points were used. The average deviation between target and model outputs was 0.24 °C with a coefficient of determination equal to 0.9966. In [22], Géczy-Víg and Farkas used the same system and data collected in the same period of [11] with the main aim of studying the effect of the sampling interval on the accuracy of the ANN-based model; in particular, sampling intervals of 1, 2, 5, 10, 30, and 60 min were considered. The average deviation between predicted and target values was reduced from 0.76 °C in the case of a sampling time of 60 min down to 0.08 °C in the case of a sampling time equal to 1 min. Kalogirou et al. [23] trained an ANN-based model of a solar domestic water-heating system integrated with a cylindrical STES to predict the useful energy that can be extracted, as well as the temperature rise in the tank. Data were collected from 33 case studies differing in terms of solar thermal collector area, open or closed system, horizonal or vertical STES, and storage capacity (which varies between 100 L and 200 L); 3 of these case studies were randomly selected for validating the ANN-based model, while the other 30 case studies were considered with the aim of training and testing the ANN-based model. The maximum percentage error corresponding to the case studies used for the ANN-based model validation ranged from 7.1% up to 9.7%. Souliotis et al. [24] combined an ANN-based model with a model developed via the dynamic simulation software TRNSYS [25] to study a STES prototype used for storing solar energy. The tank was a horizontal cylinder with a radius of 0.36 m and a length of 1.01 m. The target output of the ANN-based model was the mean storage temperature, while the month, the ambient temperature, the wind speed, the total solar irradiation on the thermal collector, and the incident angle of solar radiations were used as inputs. Both training and testing datasets included data taken during the day (when solar energy was charged) as well as during the night (where natural cooldown took place), while discharging periods were not considered. The ANN-based model was connected with the software TRNSYS to model the annual performance of the system under a typical meteorological year in Athens

(Greece). The time step for both the ANN-based model and the TRNSYS model was 30 min. Yaïci and Entchev [12] built an ANN-based model to predict the performance of a solar thermal energy system for domestic hot-water and space-heating applications by using experimental data. The system consisted of two flat-plate solar collectors, a 183 L vertical water STES, a propane-fired tank as auxiliary system, an air-handling unit, and a city water reservoir with a capacity of 1000 L. The ambient air temperature, solar irradiation, and tank temperatures at six different layers at previous time step were used as inputs, while the outputs included the above-mentioned six tank temperatures, the heat input from solar collectors, and the auxiliary heat input at the current time step. Experimental tests were conducted, with each test covering a period of 24 h with a time step of 1 min. A total of 82 summer days and 73 winter days in the period from March 2011 to December 2012 in Ottawa (Canada) were selected for developing the ANN; 70% of the data was used for training, 15% for validation, and 15% for testing. The model was developed using the MATLAB neural network toolbox [19]. Yaïci and Entchev [12] optimized the ANN architecture and found that the best learning algorithm was the Levenberg–Marquardt and the optimum number of neurons in the hidden layer was 20. The mean relative errors between the predicted and the experimental tank temperatures were within the range 1.09% ÷ 1.18% with reference to the testing dataset.

Previous studies have demonstrated the effectiveness of ANN-based models for temperature stratification prediction and energy performance estimation in TES systems [11,12,18,20–24]. However, the existing research often suffers from limitations, such as low temporal resolution, restricted operational modes, and insufficient validation against independent datasets [11,12,18,20–24]. These investigations showed significant variation in their experimental setups and methodologies. The geometric configurations of the STESs were vertical cylindrical [11,12,20–23], with some exceptions including a vertical rectangular cuboid [18] and horizontal designs [23,24]. Furthermore, a notable disparity existed in the scale of the systems, with Siahoui et al. [20] and Lee et al. [18] modeling large-scale STESs for seasonal storage (1357 m^3 and unspecified volume, respectively), while the remaining studies focused on smaller-scale systems (ranging from 0.1 m^3 [23] to 0.4112 m^3 [24]). The data used to train and validate these models also varied, with one study relying on data from physics-based models [18] and the other seven utilizing empirical data [11,12,20–24]. The experimental conditions under which data were collected were inconsistent, encompassing discharging mode only [20], both charging and discharging modes [18], natural cooldown only [21], both charging and natural cooldown [24], or normal operational use covering all modes implicitly [11,12,22] (Kalogirou et al. [23] did not specify the STES operation they tested). The measurement time steps for data acquisition ranged from 1 min [12] to 10 days [20], with one study specifically examining the effect of the time step on model performance [22]. While most studies focused on hot STESs [11,12,21–24], there are only two developed models for cold STES systems [18,20]. The modeling was performed in the MATLAB environment [19] in several cases [11,12,18,21,22], though other researchers [20,23,24] did not specify the software they utilized. In Diez et al. [21], the experimental setup was located inside a lab with almost constant ambient temperature around it, while the STESs considered in [11,12,18,20,22–24] were exposed to the real outside weather conditions. Crucially, most studies verified their models using a separate independent dataset [11,12,21–24], a practice not consistently followed across all research. Furthermore, only two studies [12,20] conducted a sensitivity analysis on both the training functions and the number of neurons in the hidden layers to optimize the ANN-based model and minimize the corresponding errors.

Wang et al. [26] introduced a short-term energy consumption forecasting approach for cold storage refrigeration systems employing long short-term memory (LSTM) neural

networks. When benchmarked against alternative models, including cascade correlation neural networks (CCNNs), bidirectional LSTM (BiLSTM), and gated recurrent units (GRUs), the LSTM-based framework exhibited superior predictive performance, achieving an improvement in the coefficient of determination (R^2) ranging from 0.306 to 0.475. Cheng et al. [27] further enhanced traditional LSTM architecture by coupling it with temporal convolutional networks (TCNs) to improve one-hour ahead single-step forecasting, while incorporating an attention mechanism to strengthen multi-step predictions over 8 h and 24 h horizons. The proposed Attention-TCN-LSTM model was evaluated against three neural network architectures and two conventional machine-learning models across multiple temporal scales. The findings indicated that the proposed approach can reduce the root mean square error (RMSE) by 17.74% to 34.26% and increase the R^2 metric by 3.54% to 9.36%. Saikia et al. [28] developed an artificial intelligence-based model grounded in nonlinear auto-regressive networks with exogenous inputs (NARX) to estimate the state of charge and outlet temperature of ice storage tanks in thermal energy networks, achieving higher accuracy and faster computation compared to physics-based models. Similarly, Badji et al. [29] applied machine-learning techniques to forecast greenhouse temperature control in Phase Change Material (PCM)-based thermal energy storage systems, where the NARX model demonstrated consistently high prediction accuracy across all evaluated scenarios. NARX explicitly models dependence on past inputs and outputs, which aligns naturally with energy balance and heat propagation, without learning opaque long-term memory mechanisms; NARX is theoretically grounded for nonlinear dynamic systems with feedback [30]. In comparison to NARX, other sequence models introduce complexity that is often unnecessary for control-oriented thermal storage applications [31]; compared to other sequence models, NARX typically requires far fewer parameters and less data to generalize well [32]. Moreover, training and deploying NARX is lightweight and robust, while LSTM/GRU/TCN often require careful architecture design, hyperparameter search, and more computation for marginal gains in this domain [28]. For STES with stratification-driven temporal dynamics, NARX offers a better bias-variance trade-off and stronger physical alignment than more recent sequence models, whose additional flexibility is often unnecessary [31].

1.2. Novelty and Goals of the Work

This study addresses critical gaps in the scientific literature. To address these gaps, this study develops a robust ANN-based predictive model for commercially available STES units using high-resolution experimental data. The proposed model aims to characterize system behavior across all operational modes (charging, discharging, heat-up, and cooldown) under both heating and cooling conditions. A comprehensive sensitivity analysis is conducted on multiple ANN architectures to identify the optimal configuration. Furthermore, the model's generalization capability is rigorously evaluated using an independent verification dataset, ensuring its applicability for real-world scenarios. The outcomes of this research provide a foundation for advanced applications such as real-time control, forecasting, fault detection, and digital twin development in building energy systems [33].

The model's foundation is a comprehensive experimental training dataset collected from 0.3 m^3 vertical cylindrical tanks (with an internal heat exchanger (IHX)) at the SENS i-Lab of the Department of Architecture and Industrial Design of the University of Campania Luigi Vanvitelli. This training dataset captures real-world thermal storage and stratification characteristics within a fully monitored environment, encompassing eight distinct operational modes: hot/cold charging, heat-up/cooldown, hot/cold discharging, simultaneous discharging/charging. These data were recorded with a high temporal resolution (5 s

or 1 min) using a water–ethylene glycol mixture (6% by volume) as a heat carrier fluid (HCF). A systematic sensitivity analysis was conducted on 28 different ANN architectures by varying the number of hidden layer neurons and the input delay; the ANN architectures were developed using the MATLAB neural network toolbox [19] by means of the training database. They were designed to predict current HCF temperatures at four internal tank levels, the tank outlet, and the IHX outlet. Inputs included the HCF temperatures at the same positions, along with the HCF temperatures and the volumetric flowrates at both the tank and IHX inlets, as well as the outside air temperature from the previous time steps. The optimal ANN configuration, designated as ANN5 (12 neurons in the hidden layer together with a delay equal to 1), was selected thanks to its best performance. The accuracy of this ANN5-based model was furthermore verified by comparing its outputs against an additional, independent experimental dataset (called the verification database) performed on the same experimental setup with a temporal resolution of 5 s, which was obtained while the STES system was actively supplying heating or cooling power to a fan coil unit in a laboratory test room. This research builds upon the previous study [33], which developed a calibrated and validated physics-based TRNSYS 18 model [25,34] of the same experimental system analyzed in this paper.

The existing literature [11,12,18,20–24] on using ANNs for dynamic modeling of STES systems reveals several limitations. Most studies have focused on vertical cylindrical units of scales varying from 0.1 m^3 to 1357 m^3. A significant gap exists in the comprehensive coverage of operational modes; previous research has often been limited to a single mode, with only a few studies encompassing all possible modes. Furthermore, research on STES operation under the cooling mode has been particularly scarce, with existing works focusing exclusively on large-scale seasonal systems (leaving a gap for short-term applications). Another key limitation of previous studies is the data resolution (which has been shown to influence model performance), with measurement time steps ranging from 1 min to 10 days. Additionally, a comprehensive parametric study to identify the optimal ANN architecture has not been a consistent feature of these studies, and a few have only performed a limited sensitivity analysis. Crucially, a significant research void exists in the rigorous verification of ANN-based models against an independent set of experimental data not used during the initial training, validation, and testing phases; this practice is essential for establishing the models' generalizability and reliability.

This work represents a significant advancement in data-driven modeling of STES systems with respect to the above-mentioned limitations considering the following:

- With respect to prior limited ANN tank-stratification studies, the proposed model covers all possible operating modes of STESs (heat-up/cooldown, charging, discharging, and simultaneous discharging/charging) under both cooling and heating operation. In addition, it is based on data measured with a reduced sampling interval (5 or 60 s); moreover, the ANN-based model developed in this study is obtained by performing a comprehensive parametric study to identify its optimal architecture and its performance is also verified against an independent experimental dataset.
- This research overcomes the limitations of physics-based/digital-twin approaches that (i) rely on simplified assumptions limiting the model accuracy when applied to realistic systems and (ii) require extensive computational resources/time and detailed information, making them quite impractical to resolve transient heat transfer and fluid dynamics within storage STESs.

The key aims of the present investigation are outlined below:

- Characterize the performance of a typical commercially available short-term STES across a comprehensive range of operating modes and boundary conditions.

- Develop, validate, and test a predictive ANN-based model that accurately captures the dynamic thermal performance of the STES using high-resolution experimental measurements.
- Conduct a detailed parametric study of 28 different ANN architectures to identify the optimal configuration for enhanced predictive accuracy.
- Provide an experimentally verified model to the scientific community for real-time control, forecasting, fault detection and diagnosis, and digital twin acceleration of typical STESs.

The paper is structured as follows. Section 2 provides a brief description of the experimental setup and testing procedures. Section 3 details the comprehensive experimental tests and the resulting dataset. The methodology for the ANN-based model is presented in Section 4, including its parameters, inputs, and outputs in Section 4.1. Section 4.2 describes the evaluation of 28 different ANN-based models. The performance of the optimal ANN configuration is then evaluated in terms of temperature prediction and energy performance in Section 4.3. The additional verification experiments simulating typical daily tanks' operations (charging, discharging, and simultaneous discharging/charging) are detailed in Section 5.1. Finally, Section 5.2 presents a comparison between the predicted outputs of the selected ANN model and the measured results from these two independent verification tests.

2. Experimental Setup

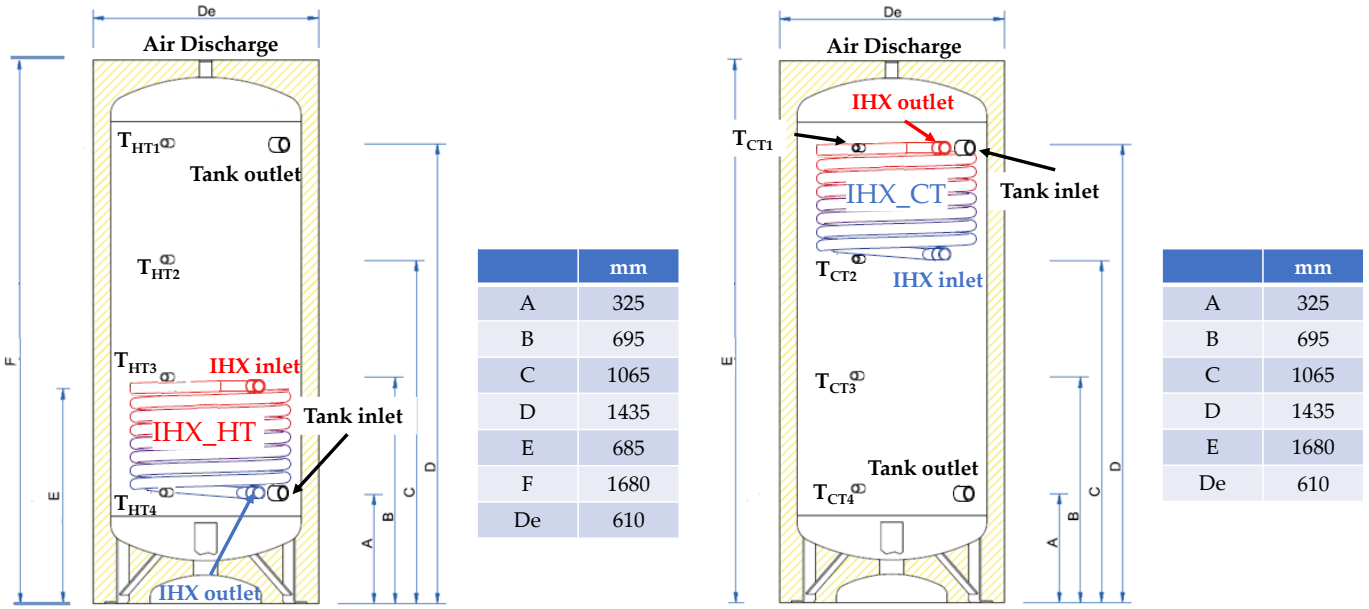
This section illustrates the experimental apparatus installed at the SENS i-Lab of the Department of Architecture and Industrial Design (located in Aversa in southern Italy) of the University of Campania Luigi Vanvitelli as well as its sensors. Figure 1 shows the setup used in this study as well as its main components.



Figure 1. Picture of the experimental apparatus of the SENS i-Lab.

The core of the experimental setup is represented by two identical vertical cylindrical tanks, where one of them is used as the hot tank (HT), while the other one is tested as the cold tank (CT). These tanks are commercially available (model PUIW-3 [35]). Both tanks consist of mild steel with rigid polyurethane insulation of 35 mm (covered by a layer of PVC); their interior volume is 0.3 m^3. Each tank contains an immersed heat exchanger (IHX) made of carbon steel; the IHX is characterized by an exterior surface area SA_{IHX} of

1 m^2 together with an outer tube diameter $D_{out,IHX}$ of 32 mm. Each tank has one outlet and one inlet. The geometry of the tanks is described in Figure 2, which also shows (i) the height and external diameter of the tanks, (ii) the heights of the tank's outlet and inlet, (iii) the IHX outlet and inlet, and (iv) the installation positions of the devices measuring the HCF temperature at four distinct heights into the CT (T_{CT1}, T_{CT2}, T_{CT3}, and T_{CT4}) as well as into the HT (T_{HT1}, T_{HT2}, T_{HT3}, and T_{HT4}). The thermal conductivity of the tank's wall is 50 W/mK, while the IHX wall thermal conductivity is 45 W/mK; the thermal conductivity of insulating material (rigid polyurethane) is 0.023 W/mK.



	mm
A	325
B	695
C	1065
D	1435
E	685
F	1680
De	610

	mm
A	325
B	695
C	1065
D	1435
E	1680
De	610

Figure 2. Geometric characteristics of the tanks: (**a**) hot tank, (**b**) cold tank.

The whole setup, described in Figure 3, is characterized by a cooling circuit (in blue) as well as a heating loop (in red). The CT is part of the cooling circuit, while the heating loop includes the HT. The HT and the CT are connected to the cold and hot loops, respectively, via their IHXs. The HCF is a mixture of water and ethylene glycol (about 6% by the volume) flowing into both loops.

An electric air-to-water heat pump (HP), with a 13.8 kW rated heating power, is connected to a 0.075 m^3 internal hot tank (IHT); the HP is run to keep the temperature within the IHT at the appropriate level. Through a closed circuit that includes pump P1 (which has a rated volumetric flowrate of 2.3 m^3/h), the IHT is linked to the internal heat exchanger of the HT (IHX_HT). A fan coil unit (FC), which is situated inside the SENS i-Lab's integrated test room for heating purposes, receives the HCF from the HT via pumps P3 and P4. An electric air-to-water refrigerating system (RS), with a rated cooling power of 13.6 kW, is connected to the 0.075 m^3 internal cold tank (ICT); the RS is turned on to keep the ICT at the appropriate temperature. Through a closed circuit that includes pump P2 (which has a rated volumetric flowrate of 2.3 m^3/h), the ICT is coupled with the internal heat exchanger of the CT (IHX_CT). Pumps P3 and P4 move the HCF from the CT into the FC, which lowers the air temperature within the SENS i-Lab's integrated test room. The inlet of the FC (which has a rated cooling power of 8.25 kW and a rated heating power of 11.68 kW [36]) can be alternatively connected to the outlet of the HT or the CT; the inlet of the HT and CT could be alternatively joined to the outlet of the FC. Eight valves (v_1, v_2, v_3, v_4, v_5, v_6, v_7, and v_8) manage the flow streams in the loops, making it possible to switch between the cooling circuit and heating circuit.

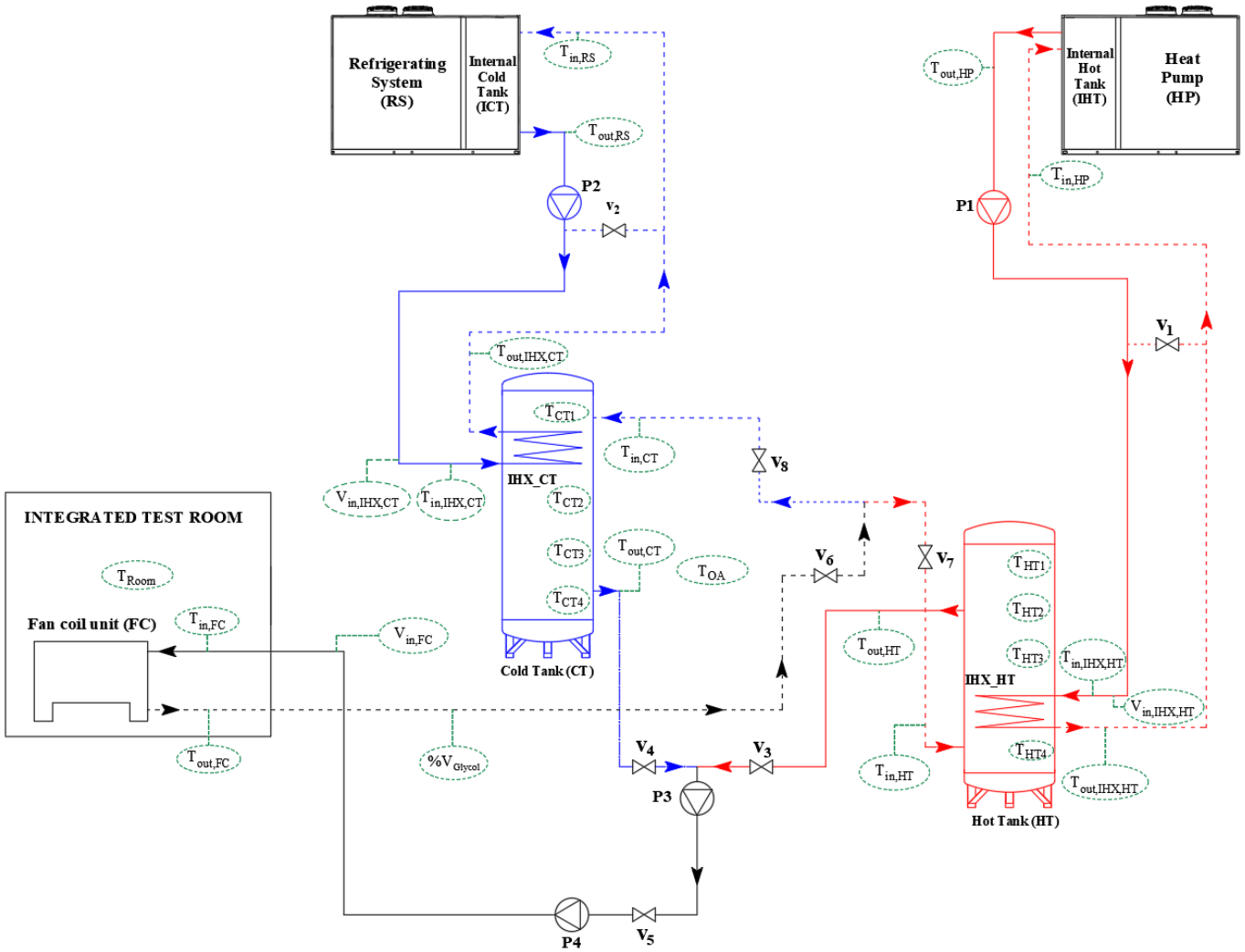


Figure 3. Schematic of the experimental setup.

The experimental setup is fully instrumented to monitor and record the key performance parameters, including (i) the HCF temperature at different levels into the CT (T_{CT1}, T_{CT2}, T_{CT3}, and T_{CT4}) and the HT (T_{HT1}, T_{HT2}, T_{HT3}, and T_{HT4}), (ii) the temperature of the HCF leaving and entering the IHX_CT ($T_{out,IHX,CT}$ and $T_{in,IHX,CT}$, respectively) and the IHX_HT ($T_{out,IHX,HT}$ and $T_{in,IHX,HT}$, respectively), (iii) the HCF temperature at the outlet and the inlet of the CT ($T_{out,CT}$ and $T_{in,CT}$, respectively) and the HT ($T_{out,HT}$ and $T_{in,HT}$, respectively), (iv) the temperature of the HCF leaving and entering the HP ($T_{out,HP}$ and $T_{in,HP}$, respectively), the RS ($T_{out,RS}$ and $T_{in,RS}$, respectively), and the FC ($T_{out,FC}$ and $T_{in,FC}$, respectively), (v) the outdoor air temperature T_{OA}, (vi) the ethylene glycol percentage $\%V_{glycol}$ of the HCF into the tanks, (vii) the HCF volumetric flowrate passing through the IHX_CT ($V_{in,IHX,CT}$), the IHX_HT ($V_{in,IHX,HT}$), and the FC ($V_{in,FC}$). The HCF volumetric flowrate passing through the FC ($V_{in,FC}$) is equal to the HCF volumetric flow entering the HT ($V_{in,HT}$) or the CT ($V_{in,CT}$); in addition, it should be underlined that the HCF volumetric flow entering the HT or the CT is equal to the HCF volumetric flow exiting the HT ($V_{out,HT}$) or the CT ($V_{out,HT}$), respectively. The measured parameters together with the measuring range and the accuracy of the sensors used in the experimental setup are detailed in Table 1. With reference to the outdoor air temperature measurement T_{OA}, it should be noted that a shielded sensor mounted at a height of 2.4 m above the ground and positioned 0.7 m away from the STES tanks has been used. In addition, it should be highlighted that all sensors have been purchased as calibrated by the corresponding manufacturers according to spe-

cific calibration protocols/standards. Further information on the experimental apparatus is provided in [33].

Table 1. Measuring range and accuracy of sensors.

Parameters	Sensor Measurement Range	Sensor Accuracy
Temperature T_{OA} of outdoor air [37]	−40 °C ÷ 60 °C	±0.2 °C at 20 °C
Temperature T_{Room} of air into the test room [38]	−10 °C ÷ 60 °C	±0.5 °C
Volumetric flowrate $V_{in,FC}$ of HCF entering the FC [39]	0.7 dm^3/s ÷ 0.88 dm^3/s	±0.34% of reading
Volumetric flowrate $V_{in,IHX,HT}$ of HCF entering the IHX_HT [39]	0.2 dm^3/s ÷ 2.46 dm^3/s	±0.33% of reading
Volumetric flowrate $V_{in,IHX,CT}$ of HCF entering the IHX_CT [39]		
Temperature $T_{in,HT}$ of the HCF at the HT inlet [40]	−4.68 °C ÷ 59.24 °C	±(0.0004·$T_{in,HT}$ + 0.0186) °C
Temperature $T_{out,HT}$ of the HCF at the HT outlet [40]		±(0.0004·$T_{out,HT}$ + 0.0186) °C
Temperature $T_{in,CT}$ of the HCF at the CT inlet [40]		±(0.0004·$T_{in,CT}$ + 0.0186) °C
Temperature $T_{out,CT}$ of the HCF at the CT outlet [40]		±(0.0004·$T_{out,CT}$ + 0.0186) °C
Temperature $T_{in,IHX,HT}$ of the HCF at the IHX_HT inlet [40]		±(0.0004·$T_{in,HT,IHX}$ + 0.0186) °C
Temperature $T_{out,IHX,HT}$ of the HCF at the IHX_HT outlet [40]		±(0.0004·$T_{out,IHX,HT}$ + 0.0186) °C
Temperature $T_{in,IHX,CT}$ of the HCF at the IHX_CT inlet [40]		±(0.0004·$T_{in,IHX,CT}$ + 0.0186) °C
Temperature $T_{out,IHX,CT}$ of the HCF at the IHX_CT outlet [40]		±(0.0004·$T_{out,IHX,CT}$ + 0.0186) °C
Temperature T_{HT1} of the HCF at the HT top node [40]		±(0.0004·T_{HT1} + 0.0186) °C
Temperature T_{HT2} of the HCF at the HT node 2 [40]		±(0.0004·T_{HT2} + 0.0186) °C
Temperature T_{HT3} of the HCF at the HT node 3 [40]		±(0.0004·T_{HT3} + 0.0186) °C
Temperature T_{HT4} of the HCF at the HT bottom node [40]		±(0.0004·T_{HT4} + 0.0186) °C
Temperature T_{CT1} of the HCF at the CT top node [40]		±(0.0004·T_{CT1} + 0.0186) °C
Temperature T_{CT2} of the HCF at the CT node 2 [40]		±(0.0004·T_{CT2} + 0.0186) °C
Temperature T_{CT3} of the HCF at the CT node 3 [40]		±(0.0004·T_{CT3} + 0.0186) °C
Temperature T_{CT4} of the HCF at the CT bottom node [40]		±(0.0004·T_{CT4} + 0.0186) °C
Temperature $T_{in,HP}$ of the HCF at the HP inlet [40]		±(0.0004·$T_{in,HP}$ + 0.0186) °C
Temperature $T_{out,HP}$ of the HCF at the HP outlet [40]		±(0.0004·$T_{out,HP}$ + 0.0186) °C
Temperature $T_{in,RS}$ of the HCF at the RS inlet [40]		±(0.0004·$T_{in,RS}$ + 0.0186) °C
Temperature $T_{out,RS}$ of the HCF at the RS outlet [40]		±(0.0004·$T_{out,RS}$ + 0.0186) °C
Temperature $T_{in,FC}$ of the HCF at the FC inlet [40]		±(0.0004·$T_{in,FC}$ + 0.0186) °C
Temperature $T_{out,FC}$ of the HCF at the FC outlet [40]		±(0.0004·$T_{out,FC}$ + 0.0186) °C
Percentage by volume $\%V_{glycol}$ of glycol in the HCF [41]	0 ÷ 100%	±0.5% of reading

Two independent datasets have been developed: the "training database" that has been used to train, validate, and test the 28 ANN architectures analyzed in Section 4 and the "verification database" that is used to verify the performance of the optimal ANN5-based model.

3. Experimental Training Tests

Four distinct independent experiments were conducted on both the HT and the CT to investigate the four major operational modes of the STESs. These tests included the following: (i) a heat-up experiment for the HT and a cooldown experiment for the CT; (ii) a dedicated charging test for both tanks; (iii) a dedicated discharging test for both tanks; (iv) a test with simultaneous discharging/charging of the HT and the CT. Each experiment was conducted under transient outdoor conditions, and the duration of each test was set to achieve a steady-state condition in the tanks. This steady-state condition was operationally defined as the point at which the temperature difference between the current measurement at any tank node and the arithmetic mean of the associated temperatures over

the preceding 30 min was less than 0.2 °C. The resulting experimental dataset (called the training database) for the CT and the HT are presented in Sections 3.1 and 3.2, respectively, and was used to train, validate, and test the 28 ANN architectures presented in Section 4. Additional details regarding the experimental tests can be found in [33].

3.1. Experimental Training Tests on the Cold Tank

Table 2 summarizes the experimental details for the natural heat-up, charging, discharging, and simultaneous discharging/charging of the independent training experiments of the CT, including the starting date/time, the ending date/time, the total test duration, the number of recorded samples, and the corresponding sampling interval.

Table 2. Dataset summary of the four CT training tests.

	Natural Heat-Up Experiment	Charging Experiment	Discharging Experiment	Simultaneous Discharging/Charging Experiment
Starting date (dd/mm/yyyy)	09/05/2022	06/05/2022	20/04/2022	21/04/2022
Starting time (hh:mm:ss)	18:24:08	09:38:29	15:03:12	13:10:36
Ending date (dd/mm/yyyy)	15/05/2022	06/05/2022	20/04/2022	21/04/2022
Ending time (hh:mm:ss)	02:43:38	18:35:26	18:59:51	18:46:47
Total duration (min)	7699.0	529.5	233.0	331.0
Number of samples	7700	6355	2797	3973
Sampling interval (s)	60	5	5	5

The natural heat-up experiment of the CT corresponds to the time during which the CT stores the maximum possible energy, in the absence of cooling energy demand. During this test, the CT was initially fully charged via the cold HCF (flowing through the IHX_CT) provided by the RS (operating constantly during the entire workday) at the lowest attainable homogeneous temperature (around 8 °C); then, the test was initiated by maintaining both the CT outlet/inlet and the IHX_CT outlet/inlet completely closed through the whole duration of the test. Figure 4 reports the HCF temperatures at the four distinct nodes of the CT (T_{CT1}, T_{CT2}, T_{CT3}, and T_{CT4}) as well as the temperature of outdoor air around the CT (T_{OA}) upon varying the time during the whole experiment.

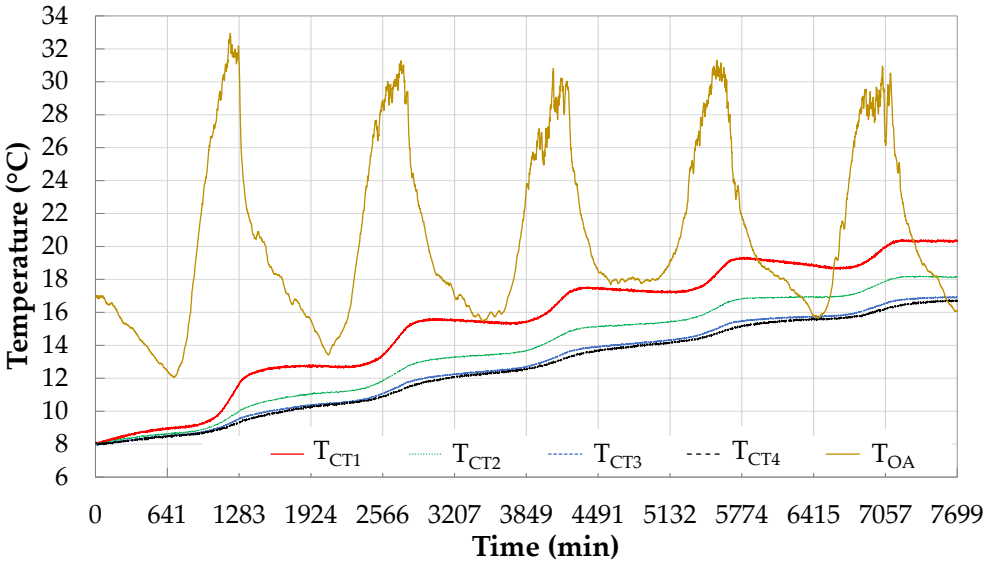
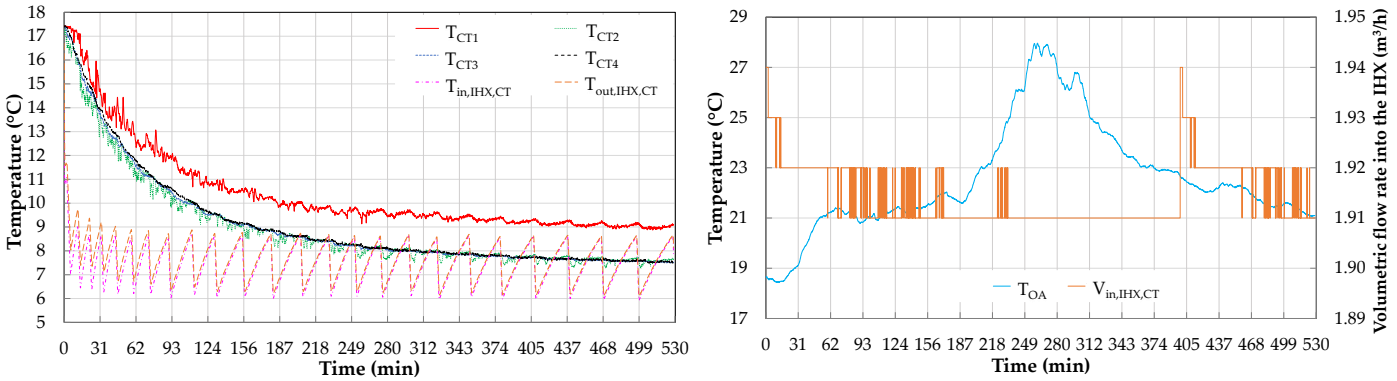


Figure 4. HCF temperatures at the four distinct nodes of the CT (T_{CT1}, T_{CT2}, T_{CT3}, and T_{CT4}) and outside air temperature (T_{OA}) in the case of the natural heat-up experiment of the CT.

The charging experiment of the CT represents the time during which cooling energy is stored in the CT, while cooling energy is not required. During this experiment, the CT was initially filled via the HCF (with a homogeneous temperature of around 17.5 °C) achieved after three days of not using the CT. Following that, the RS was activated and the charging experiment of the CT was initiated by moving the cold HCF (provided by the RS) into the IHX_CT during the whole duration of the experiment, while both the outlet and inlet of the CT were always kept fully closed. Figure 5a shows the measured HCF temperatures (T_{CT1}, T_{CT2}, T_{CT3}, and T_{CT4}) at the four distinct nodes of the CT and the HCF temperature exiting ($T_{out,IHX,CT}$) and entering ($T_{in,IHX,CT}$) the IHX_CT upon varying the time; the temperature (T_{OA}) of the outdoor air around the CT as well as the volumetric flowrate ($V_{in,IHX,CT}$) of the HCF passing through the IHX_CT are indicated in Figure 5b.



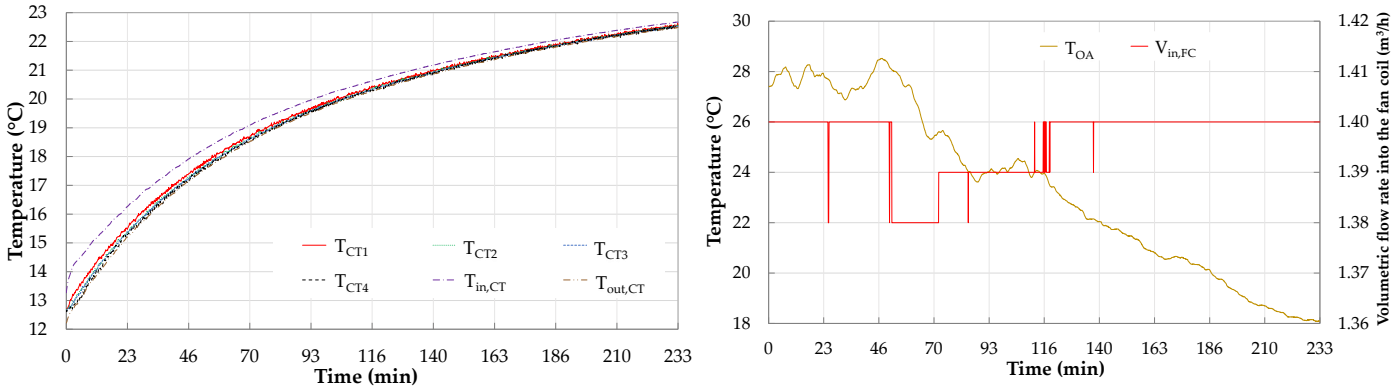
(**a**) (**b**)

Figure 5. Measured HCF temperatures at the four distinct nodes (T_{CT1}, T_{CT2}, T_{CT3}, and T_{CT4}) of the CT as well as at the inlet/outlet of the IHX_CT ($T_{in,IHX,CT}$ and $T_{out,IHX,CT}$) (**a**); outside air temperature (T_{OA}) and volumetric flowrate ($V_{in,IHX,CT}$) of the HCF flowing into the IHX_CT (**b**) during the CT charging experiment.

During the discharging experiment of the CT, cooling energy is required but it is not stored. In this experiment, the CT was initially filled via the HCF, exhibiting a homogeneous temperature of around 12.5 °C (which was the minimum achievable temperature while operating the RS constantly for approximately four hours to finish the experiment within the workday); then, the test was initiated by completely closing both the inlet and the outlet of the IHX_CT during the entire experiment, while always keeping the inlet and the outlet of the CT (coupled with the FC) open. The cold HCF stored in the CT was moved into the FC to lower the air temperature within the test room. Figure 6a describes the measured HCF temperatures (T_{CT1}, T_{CT2}, T_{CT3}, and T_{CT4}) at the four distinct nodes of the CT, as well as the HCF temperature entering ($T_{in,CT}$) and exiting ($T_{out,CT}$) the CT; the temperature (T_{OA}) of the outside air around the CT together with the volumetric flowrate ($V_{in,FC}$) of the HCF flowing through the FC are indicated in Figure 6b upon varying the time.

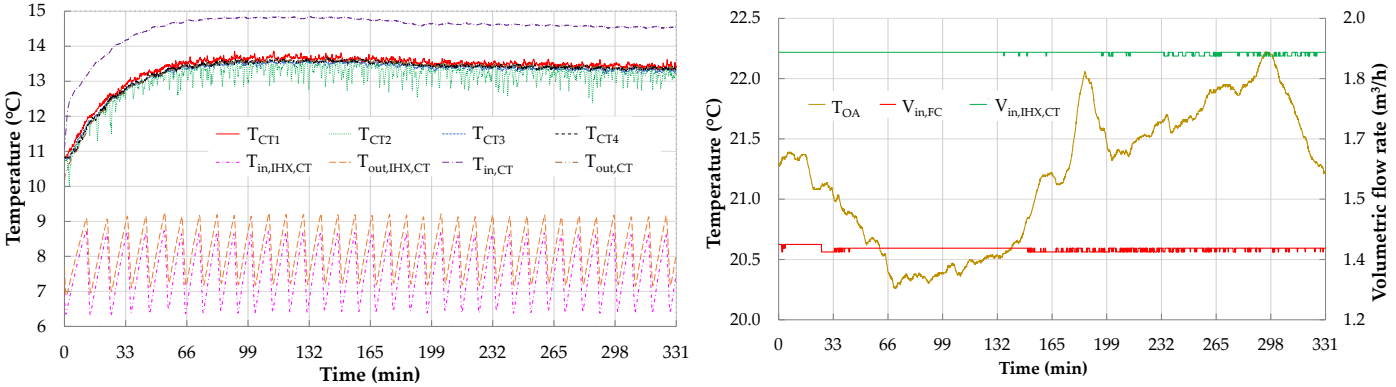
The simultaneous discharging/charging experiment of the CT corresponds to the time during which cooling energy is simultaneously stored into the CT and provided to end-users. During this experiment, the CT was initially filled via the HCF, characterized by a homogeneous temperature of around 11 °C (which represented the minimum achievable temperature while running the RS constantly for approximately four hours to finish the test within the workday); then, the RS was turned on and the test was initiated by completely opening both the outlet and the inlet of the IHX_CT (linked to the RS) as well as both the outlet and the inlet of the CT (linked to the FC) during the entire experimental test. Figure 7a reports the measured HCF temperatures (T_{CT1}, T_{CT2}, T_{CT3}, and T_{CT4}) at the four distinct nodes of the CT, the HCF temperature exiting ($T_{out,IHX,CT}$) and entering ($T_{in,IHX,CT}$) the IHX of the CT, and the HCF temperature exiting ($T_{out,CT}$) and entering ($T_{in,CT}$) the CT,

while Figure 7b shows the temperature (T_{OA}) of outdoor air around the CT, the volumetric flowrate ($V_{in,FC}$) of the HCF flowing through the FC, and the volumetric flowrate ($V_{in,IHX,CT}$) of the HCF passing into the IHX_CT upon varying the time.



(**a**) (**b**)

Figure 6. Measured HCF temperatures at the four distinct nodes of the CT (T_{CT1}, T_{CT2}, T_{CT3}, and T_{CT4}) as well as at the inlet/outlet of the CT ($T_{in,CT}$ and $T_{out,CT}$) (**a**); temperature of outside air (T_{OA}) and volumetric flowrate of the HCF flowing into the FC ($V_{in,FC}$) (**b**) over the discharging experiment of the CT.



(**a**) (**b**)

Figure 7. Measured HCF temperatures (T_{CT1}, T_{CT2}, T_{CT3}, T_{CT4}, $T_{in,IHX,CT}$, $T_{out,IHX,CT}$, $T_{in,CT}$, and $T_{out,CT}$) (**a**); temperature of outside air (T_{OA}) and volumetric flowrate of the HCF flowing through the FC system ($V_{in,FC}$) and the IHX_CT ($V_{in,IHX,CT}$) (**b**) during the simultaneous discharging/charging experiment.

3.2. Experimental Training Tests on the Hot Tank

Table 3 reports a detailed description of the natural cooldown, the charging, the discharging and the simultaneous discharging/charging of the independent training experiments of the HT, including the starting date/time, the ending date/time, the total test duration, the number of recorded samples, and the corresponding sampling interval.

The natural cooldown test was designed to quantify the passive thermal energy loss of the HT when fully charged and isolated from any thermal energy demand. During this experiment, the HT was first brought to a state of maximum energy storage by circulating hot HCF supplied by a heat pump, through the IHX_HT, until a homogeneous temperature of approximately 48 °C was achieved. Subsequently, the test commenced with all inlets and outlets for both the HT and the IHX_HT being completely closed for the whole test duration. Figure 8 indicates the HCF temperatures at the four distinct vertical nodes within the HT (T_{HT1}, T_{HT2}, T_{HT3}, and T_{HT4}) and the outdoor air temperature (T_{OA}) around the HT upon varying the time.

Table 3. Dataset summary of the four HT training tests.

	Natural Cooldown Experiment	Charging Experiment	Discharging Experiment	Simultaneous Discharging/Charging Experiment
Starting date (dd/mm/yyyy)	13/04/2022	05/05/2022	11/04/2022	12/04/2022
Starting time (hh:mm:ss)	11:43:35	09:25:02	13:18:38	12:15:28
Ending date (dd/mm/yyyy)	18/04/2022	05/05/2022	11/04/2022	12/04/2022
Ending time (hh:mm:ss)	17:28:27	16:13:30	18:34:23	17:57:27
Total duration (min)	7559.0	403.0	312.0	337.0
Number of samples	7560	4837	3745	4045
Sampling interval (s)	60	5	5	5

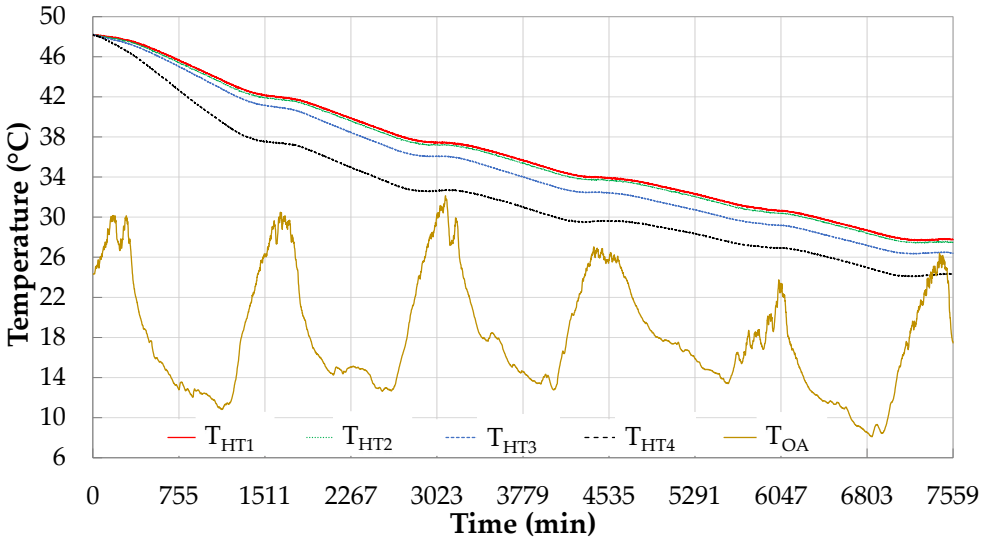
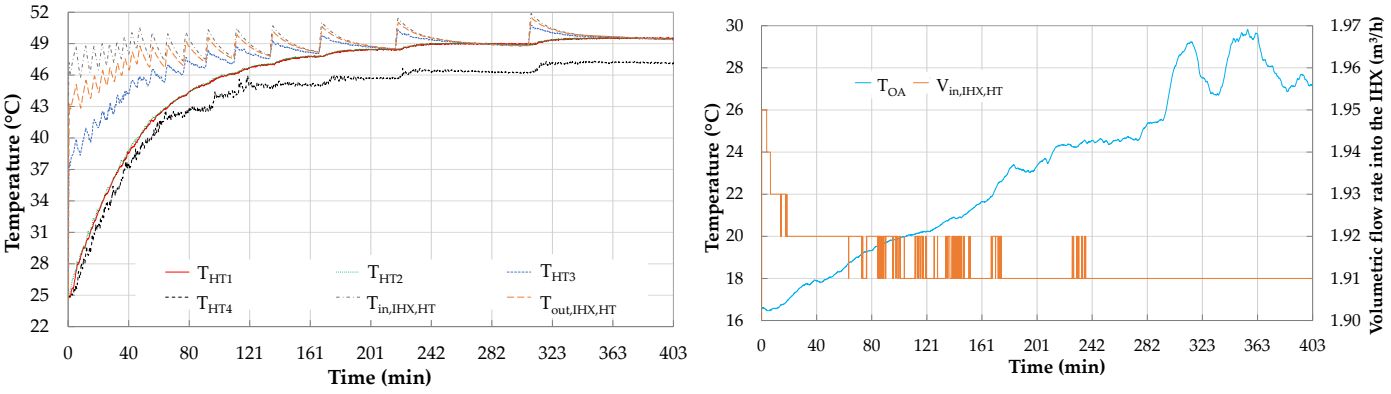


Figure 8. HCF temperatures at the four distinct vertical nodes of the HT (T_{HT1}, T_{HT2}, T_{HT3}, and T_{HT4}) and outdoor air temperature (T_{OA}) during the natural cooldown experiment of the HT.

The charging experiment of the HT was conducted to represent an energy storage period with no concurrent thermal demand. The experiment began with the HT filled with an HCF at a homogeneous temperature of around 25 °C. This initial condition was chosen to be consistent with similar charging tests in a previous study by Angrisani et al. [42] performed with a temperature of approximately 21 °C at the lowest node and around 27 °C at the highest node. The initial temperature is also close to the temperature (approximately 23 °C) used by Nash et al. [43]. Once the initial temperature was achieved, the HP was activated, and the charging of the HT was initiated by circulating the hot HCF through the IHX_HT during the whole experiment. Throughout the experiment, both the outlet and inlet of the HT were kept fully closed. The HCF temperatures at four distinct vertical nodes within the HT (T_{HT1}, T_{HT2}, T_{HT3}, and T_{HT4}), along with the temperatures at the IHX inlet ($T_{in,IHX,HT}$) and outlet ($T_{out,IHX,HT}$), are measured upon varying the time (Figure 9a). Simultaneously, the outdoor air temperature (T_{OA}) around the HT and the volumetric flowrate ($V_{in,IHX,HT}$) of the HCF through the IHX_HT are also recorded over time (Figure 9b).

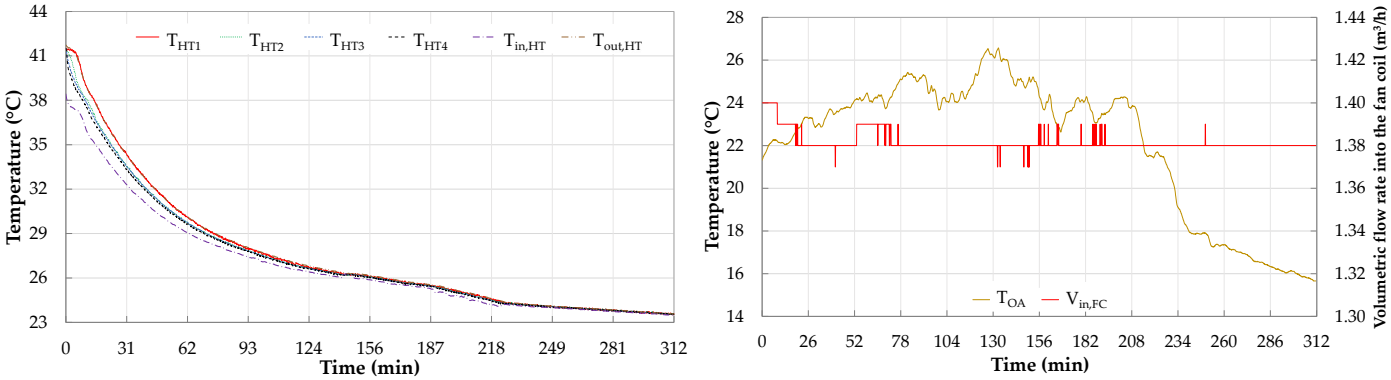
The discharging experiment of the HT represents the time during which thermal energy is required without a simultaneous charging event. During this experiment, the HT was initially filled thanks to the HCF and achieved a homogeneous temperature of around 41 °C. This initial condition was selected to be consistent with the initial temperature range (38 °C ÷ 48 °C) used in similar discharging tests carried out by Nash et al. [43]. An initial temperature of around 41 °C was achieved by operating the HP constantly for around four hours to finish the experiment within the workday. Subsequently, the test initiated with both the outlet and the inlet of the IHX_HT fully closed. Concurrently, the HT's main inlet

and outlet, which were connected to a fan coil unit (FC), were kept open for the whole test duration, allowing the stored hot HCF to circulate and provide space heating. Figure 10a shows the measured HCF temperatures at the four nodes of the HT (T_{HT1}, T_{HT2}, T_{HT3}, and T_{HT4}), as well as the HCF temperature entering ($T_{in,HT}$) and exiting ($T_{out,HT}$) the HT. Figure 10b shows the outside air temperature (T_{OA}) around the HT and the volumetric flowrate of the HCF flowing through the FC ($V_{in,FC}$) upon varying the time.



(**a**) (**b**)

Figure 9. Measured HCF temperatures at the four nodes (T_{HT1}, T_{HT2}, T_{HT3}, and T_{HT4}) of the HT as well as at the inlet/outlet of the IHX_HT ($T_{in,IHX,HT}$ and $T_{out,IHX,HT}$) (**a**); temperature of outdoor air (T_{OA}) and volumetric flowrate of HCF flowing into the IHX_HT ($V_{in,IHX,HT}$) (**b**) during the charging experiment of the HT.

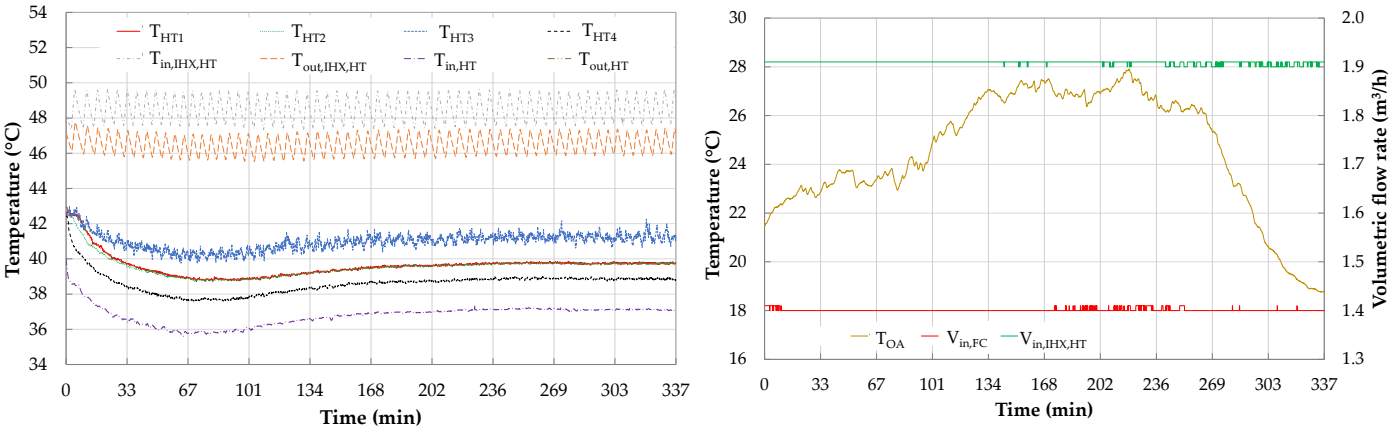


(**a**) (**b**)

Figure 10. Measured HCF temperatures at the four nodes of the HT (T_{HT1}, T_{HT2}, T_{HT3}, and T_{HT4}) as well as at the inlet/outlet of the HT ($T_{in,HT}$ and $T_{out,HT}$) (**a**); temperature of outdoor air (T_{OA}) and volumetric flowrate of the HCF flowing into the FC ($V_{in,FC}$) (**b**) over the HT discharging experiment.

The simultaneous discharging/charging experiment of the HT represents the time during which thermal energy is simultaneously stored into the tank and supplied to end-users. During this experiment, the HT was initially filled with the HCF and achieved a homogeneous temperature of around 43 °C. This temperature level was selected to be consistent with the initial conditions used in the similar simultaneous discharging/charging experiment carried out by Nash et al. [43], which featured a temperature range of 38 °C to 41 °C. The initial temperature of around 43 °C was reached by operating the HP constantly for around four hours (to finish the experiment within the workday). The test then initiated with the HP activated, as well as both the outlet and the inlet of the IHX_HT (interfaced with the HP) and both the outlet and the inlet of the HT (connected to the FC) fully opened for the duration of the experiment. Figure 11a shows the measured HCF temperatures at the four distinct nodes (T_{HT1}, T_{HT2}, T_{HT3}, and T_{HT4}) of the HT, the HCF temperature

leaving ($T_{out,IHX,HT}$) and entering ($T_{in,IHX,HT}$) the IHX_HT, and the HCF temperature exiting ($T_{out,HT}$) and entering ($T_{in,HT}$) the HT. Figure 11b presents the corresponding measurements of the outdoor air temperature (T_{OA}) of the hot tank together with both the volumetric flowrate ($V_{in,FC}$) of the HCF passing through the FC and the volumetric flowrate ($V_{in,IHX,HT}$) of the HCF passing into the IHX_HT upon varying the time.



(**a**) (**b**)

Figure 11. Measured HCF temperatures (T_{HT1}, T_{HT2}, T_{HT3}, T_{HT4}, $T_{in,IHX,HT}$, $T_{out,IHX,HT}$, $T_{in,HT}$, and $T_{out,HT}$) (**a**); temperature of outdoor air (T_{OA}) and volumetric flowrate of the HCF flowing through the FC system ($V_{in,FC}$) and the IHX_HT ($V_{in,IHX,CT}$) (**b**) during the HT simultaneous discharging/charging experiment.

4. ANN Models

The predictive model was developed using the MATLAB Neural Network Toolbox [19], with the primary objective of accurately forecasting temperature stratification within the storage tanks and temperatures at both the tank outlet and the internal heat exchanger outlet. The approach adopted in this study is based on a nonlinear auto-regressive model with exogenous inputs (NARX), which is well-suited for dynamic systems exhibiting temporal dependencies. The ANN was initially trained, validated, and tested by using the dataset collected from experimental tests for both HT and CT, as described in Section 4. To further establish the model's robustness, its predictive accuracy is subsequently verified against an independent dataset acquired during the tank's operation as an integrated component of a full heating/cooling system, as depicted in Figure 3.

4.1. Architectures of ANN Models

The NARX-based ANN predicts the system's outputs at the current time step by leveraging both previous outputs (responses) and previous inputs (predictors) within a specified delay window. The NARX model is mathematically represented by the following relationship between the response y(t) and the predictors:

$$y(t) = f(x(t-1), \ldots, x(t-d), y(t-1), \ldots, y(t-d)) \quad (1)$$

where f is the nonlinear function learned by the ANN during the training process.

For each tank, the model responses, or target outputs, include six key temperature measurements:

- The HCF temperatures at the four distinct vertical nodes into the CT (T_{CT1}, T_{CT2}, T_{CT3}, and T_{CT4}) and the HT (T_{HT1}, T_{HT2}, T_{HT3}, and T_{HT4});
- Response 5 is the HCF temperature at the IHX exit of the CT and HT ($T_{out,IHX,CT}$ and $T_{out,IHX,HT}$, respectively);

- Response 6 corresponds to the temperature at the CT and HT outlets (respectively, $T_{out,CT}$ and $T_{out,HT}$).
- The following five primary predictor variables for both the CT and the HT have been used as predictors:
- Predictor 1 represents the temperature at the IHX inlet of both the CT and the HT ($T_{in,IHX,CT}$ and $T_{in,IHX,HT}$, respectively);
- Predictor 2 corresponds to the flowrate at the IHX inlet of both cold and hot tank ($V_{in,IHX,CT}$ and $V_{in,IHX,HT}$, respectively);
- Predictor 3 is the temperature at the CT and HT inlet (respectively $T_{in,CT}$ and $T_{in,HT}$);
- Predictor 4 represents the HCF volumetric flowrate at the tank exit, which is equal to the HCF volumetric flowrate flowing into the FC ($V_{in,FC}$);
- Predictor 5 corresponds to the outdoor air temperature T_{OA}.

This means that the model has 11 inputs, which are the above-mentioned predictors and responses, and 6 outputs, which are the above-mentioned responses. Figure 12 highlights the inputs and outputs of the ANN model, as well as the model's architecture.

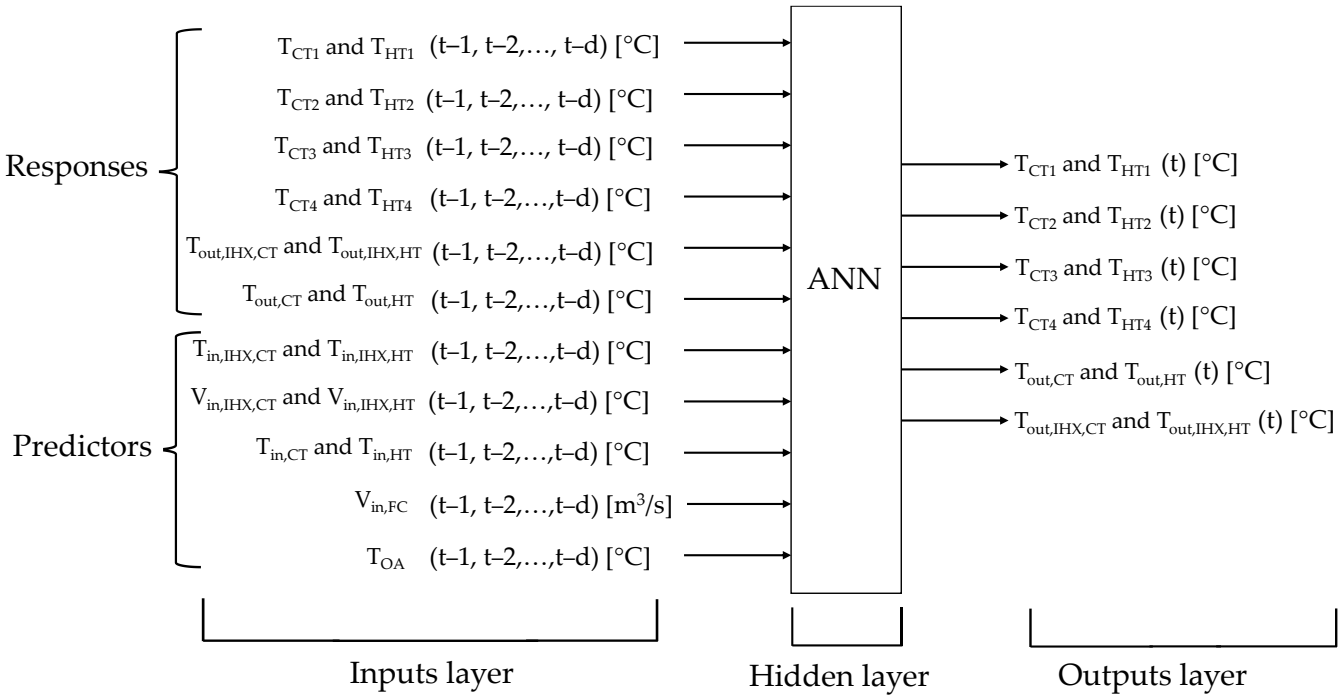


Figure 12. Architectures of the 28 ANN models.

The selection of the model inputs was based on the physical behavior of the system governing transient thermal dynamics. $V_{in,FC}$ characterizes the cooling/heating load going towards the end-user, which directly affects thermal energy discharge. $V_{in,IHX}$ and $T_{in,IHX}$ represent the thermal energy that is being charged into the tanks via the IHX, and they are the primary drivers of dynamic change; as noted in Section 5.2, the largest model deviations occur during rapid flowrate fluctuations. The IHX and tank inlet temperatures define the thermal potential being introduced to the system; they are essential for the model to identify the system operation (heating or cooling) and the magnitude of the thermal gradient. The temperature at the tanks' inlet represents an active boundary condition that directly affects the four tank nodes' temperatures. The temperatures at the four internal nodes and the two outlets from the previous time steps are the most critical for maintaining the model's memory; they capture the system's thermal inertia, which is the primary driver of temperature at any given time step due to the large thermal mass capacity of the tanks. T_{OA} is essential for characterizing the passive thermal energy exchange between the tanks

and the surrounding environment; taking into account that the tanks are not adiabatic (even if they are insulated), T_{OA} is the sole driver of temperature change during the natural cooldown and natural heat-up training experiments (even if its impact is slower compared to active flowrates). The selected network has one input layer, one hidden layer, and one output layer. The transfer function is a sigmoid function in the hidden layer and a linear function in the output layer. Levenberg–Marquardt algorithm has been adopted for training, and the performance parameter is the mean square error (which means that the ANN is trained to produce the lowest possible MSE). The training process is in open-loop, and it was implemented by setting a maximum limit of 1000 epochs. To ensure the network did not overfit the training data, an early stopping patience of six validation checks was applied which means that the training was automatically stopped if the validation MSE did not decrease for six consecutive iterations. Initial weights and biases were assigned using the Nguyen–Widrow initialization, which is the default option in the MATLAB environment for sigmoid hidden layers. This method distributes the initial active regions of the neurons evenly across the input space, leading to faster and more stable convergence. The experimental dataset was partitioned into training (70%), validation (15%), and testing (15%) subsets, following best practices in similar studies [12,18]. Data allocation was performed randomly by the MATLAB Neural Network Toolbox at the sample level to maintain statistical representativeness. During training, the toolbox employs an early stopping criterion based on the validation performance to prevent overfitting, ensuring that the final weights correspond to the minimum validation error rather than the minimum training error.

To optimize the network architecture, 28 distinct ANN configurations (labeled ANN1 through ANN28) are systematically developed and analyzed using the MATLAB Neural Network Toolbox [19] of the STESs. The only parameters varied across these networks are the number of neurons in the single hidden layer and the input delay. The specific architectures for each of the 28 models are detailed in Table 4, which highlights the number of hidden layer neurons and the corresponding delay.

All ANN models are trained, validated, and tested on a combined experimental dataset from both the CT and the HT, intentionally disregarding the distinction between tank types. The decision to combine the datasets from both cold and hot tanks into a single training dataset was based on both physical and methodological justifications. From a physical point of view, the experimental setup consists of two vertical cylindrical tanks with identical volume, construction, insulation, and sensor type and placement. Because the physical geometry and sensor type/placement are identical, the underlying thermal dynamics, such as stratification and heat losses, follow the same physical laws in both tanks. From a methodological point of view, training on a combined dataset allows the ANNs to learn the fundamental relationship between inputs and the resulting nodes' temperatures across a much wider temperature gradient than if they were trained on a single tank (this prevents the model from being limited to a specific temperature range and instead forces it to learn the universal physics of sensible heat storage). The data from the various operational modes described in Section 3 were concatenated in a specific sequence for this purpose. Data were combined as discrete, chronological experimental blocks rather than shuffled at the row level, taking into account that shuffling individual data points can destroy the temporal memory necessary for the network to learn about thermal inertia of the tanks (an early stopping criterion during training was employed to prevent the model from simply memorizing transitions within the sequence). This approach is employed to assess the model's capacity to generalize and accurately predict the temperature outputs for a generic STES, independent of its designated hot or cold thermal duty.

Table 4. Architectures of the 28 ANN models.

ANN-Based Model ID	Number of Neurons in the Hidden Layer	Delay
ANN1	8	1
ANN2	8	2
ANN3	8	4
ANN4	8	6
ANN5	12	1
ANN6	12	2
ANN7	12	4
ANN8	12	6
ANN9	16	1
ANN10	16	2
ANN11	16	4
ANN12	16	6
ANN13	20	1
ANN14	20	2
ANN15	20	4
ANN16	20	6
ANN17	24	1
ANN18	24	2
ANN19	24	4
ANN20	24	6
ANN21	28	1
ANN22	28	2
ANN23	28	4
ANN24	28	6
ANN25	32	1
ANN26	32	2
ANN27	32	4
ANN28	32	6

4.2. Performance of ANN Models vs. The Experimental Training Database

The ANN architecture consisted of one input layer, a single hidden layer, and one output layer. A total of 28 ANN configurations were evaluated using combined datasets from both hot and cold tanks. Table 4 shows performance metrics including the error ($\Delta T_{Err,i}$), average error (AE), average absolute error (ABE), mean square error (MSE), root mean square error (RMSE), normalized RMSE (NRMSE), and the coefficient of determination (R^2). These errors are calculated using the equations provided below and the values are detailed in Tables A1–A3 in Appendix A for the above-mentioned ANN models:

$$\Delta T_{Err,i} = T_{ANN,i} - T_{exp,i} \quad (2)$$

$$AE = \frac{\left(\sum_{i=1}^{N} \Delta T_{Err,i}\right)}{N} \quad (3)$$

$$ABE = \frac{\sum_{i=1}^{N} |\Delta T_{Err,i}|}{N} \quad (4)$$

$$MSE = \frac{\sum_{i=1}^{N} (\Delta T_{Err,i})^2}{N} \quad (5)$$

$$RMSE = \sqrt{\sum_{i=1}^{N} (\Delta T_{Err,i})^2 / N} \quad (6)$$

$$NRMSE = \frac{RMSE}{(T_{exp,max} - T_{exp,min})} \quad (7)$$

$$R^2 = 1 - \frac{\sum_{i=1}^{N} \left(T_{exp,i} - T_{ANN,i}\right)^2}{\sum_{i=1}^{N} \left(T_{exp,i} - \overline{T}_{exp}\right)^2} \quad (8)$$

where N represents the overall number of measured points, $T_{exp,i}$ and $T_{ANN,i}$, respectively, which are the measured and the predicted temperatures at time step i, $\overline{T}_{exp}$ is the arithmetic mean of temperatures measured during the entire test duration, and $T_{exp,max}$ and $T_{exp,min}$ are the highest and the lowest recorded temperatures during the experiments, respectively.

Tables A1–A3 in Appendix A show the values of the above-mentioned metrics for each of the six outputs associated with each of the 28 ANN models; taking into account that the ANN models have been trained, validated, and tested based on the combined experimental datasets of both the CT and the HT; the values reported in Tables A1–A3 are identical for both STESs. The best and worst performances within each row are highlighted to facilitate comparison in Tables A1–A3. The results in this table show the following:

- All of the ANN models achieve very high performances.
- The best value of AE is 0 °C and is recorded in the case of ANN1 for node 3, while the worst AE is $3342 \cdot 10^{-5}$ °C recorded in the case of ANN23 for the same node 3.
- The best ABE is $5 \cdot 10^{-3}$ °C for node 4 in the case of ANN5 and for the outlet of the tank in the case of ANN3, ANN5, and ANN21, while the worst ABE is $41 \cdot 10^{-3}$ °C achieved in the case of ANN27 at the outlet of the IHX.
- The best value of MSE is $5 \cdot 10^{-5}$ °C^2 in the case of ANN5 for both node 4 and the outlet of the tank, while the worst MSE is $1612 \cdot 10^{-5}$ °C^2 corresponding to the case of ANN16 at the outlet of the IHX.
- The best RMSE is $7 \cdot 10^{-3}$ °C for both node 4 and the outlet of the tank in the case of ANN5, while the worst RMSE is $127 \cdot 10^{-3}$ °C obtained at the IHX outlet for ANN16; in comparison to the other ANN architectures, the ANN5-based model provides the highest values of RMSE for nodes 1, 2, and 4, as well as the outlet of the tank.
- The best NRMSE is $2 \cdot 10^{-4}$ achieved in the case of ANN5 for nodes 1, 2, and 4, as well as the outlet of the tank. The same value is obtained in the case of ANN21 for node 2 and the tank outlet, as well as in the case of ANN2, ANN18, and ANN22 at the tank outlet; the worst NRMSE is $28 \cdot 10^{-4}$ recorded at the IHX outlet for ANN16.
- R^2 value is always larger than 0.9999273 for all temperatures, regardless of the number of neurons in the hidden layer as well as the delay value. The highest value of R^2 is obtained with ANN5 for nodes 1, 2, and 4, as well as the outlet of the tank.

Since near-perfect accuracy was achieved with a shallow structure, increasing the number of hidden layers would provide no measurable gain in predictive power. On the other hand, a single hidden layer requires significantly fewer weight optimizations and shorter training times than a deeper architecture (multi-hidden layers). That is why only single hidden layer architectures were investigated.

The results presented in Tables A1–A3 demonstrate that the ANN5 architecture consistently achieved the best values of RMSE, NRMSE, and R^2 at tank nodes 1, 2, and 4 as well as the tank outlet, while the ANN1 architecture showed the best performance in terms of RMSE, NRMSE, and R^2 for tank node 3 and the IHX outlet. Taking into account that in this research RMSE, NRMSE, and R^2 are considered the most significant metrics and that ANN5 achieved the best values of these metrics with reference to the majority of measurement points (4 out of 6), the overall analysis led to the selection of ANN5 as the optimal network architecture for this study.

4.3. Performance of the ANN5 Model vs. The Experimental Training Database

To identify the optimal ANN configuration, a comprehensive parametric study was conducted on 28 architectures, varying the number of neurons in the hidden layer (8–32)

and the input delay (1–6). These configurations, labeled ANN1 through ANN28, were systematically evaluated using combined datasets from both hot and cold tanks. The decision to merge datasets was based on the physical similarity of the tanks and the methodological advantage of exposing the network to a broader temperature range, thereby improving generalization. The ANN5 architecture was selected as the optimal configuration based on its consistent superiority across key metrics. The performance of ANN5 has been further assessed by comparing the predicted and the measured temperatures via the parameter $\Delta T_{Err,i}$ defined by Equation (2) for each of the six outputs defined in Section 4.1 as a function of the experiment for both tanks. The positive sign of $\Delta T_{Err,i}$ means that ANN5 overestimates the measured values and vice versa. Figure 13 shows the values of $\Delta T_{Err,i}$ for the hot tank upon varying the type of experimental test, while Figure 14 reports the values of $\Delta T_{Err,i}$ for the cold tank upon varying the type of experiment.

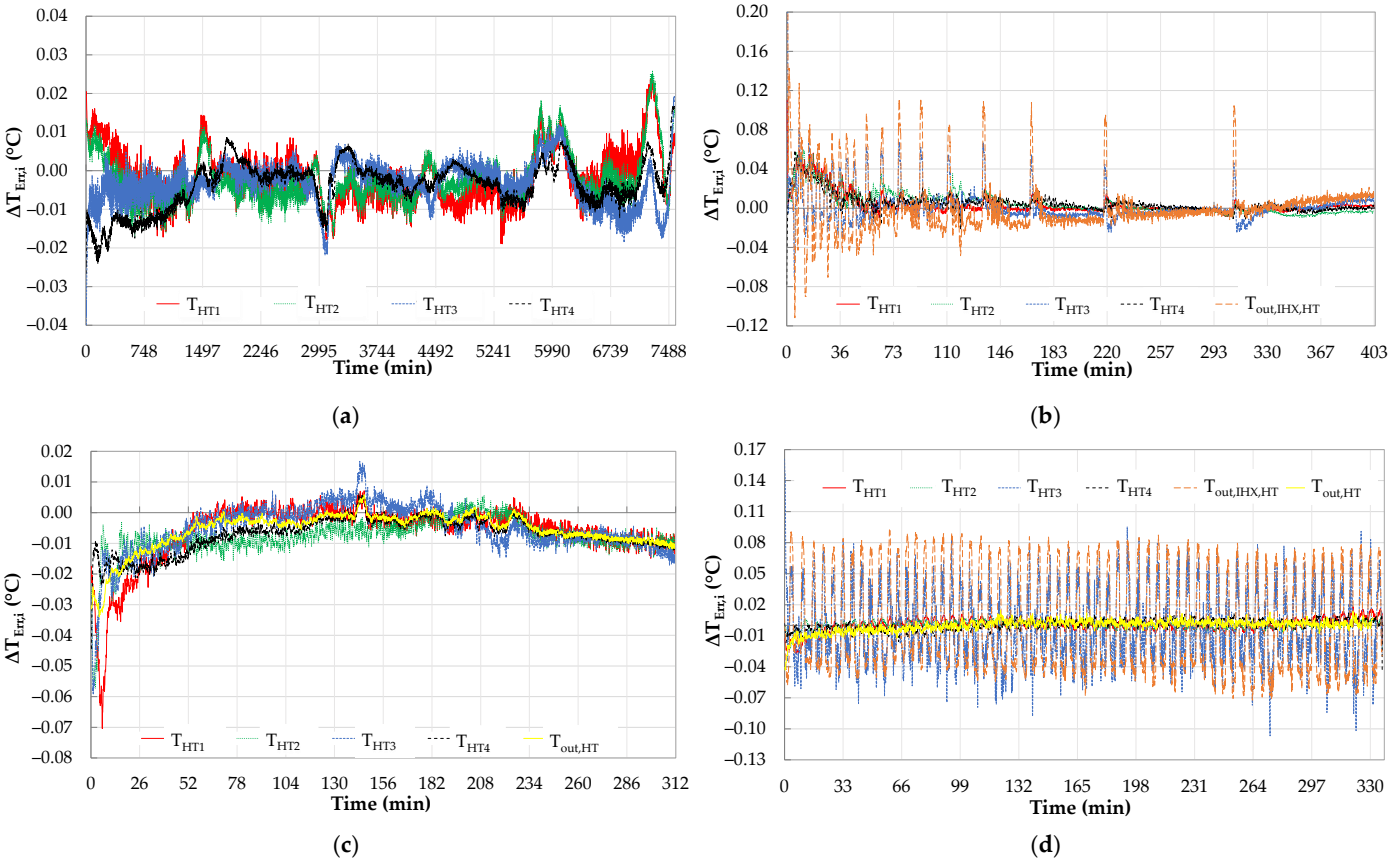


Figure 13. Values of $\Delta T_{Err,i}$ for ANN5 upon varying the time during the training experiments for the HT: (**a**) cooldown experiment, (**b**) charging experiment, (**c**) discharging experiment, (**d**) simultaneous discharging/charging experiment.

These figures highlight the following:

- Regarding the cooldown experiment of the HT (Figure 13a), $\Delta T_{Err,i}$ stays within the range -0.025 °C ÷ 0.025 °C for nodes 1, 2, 3, and 4.
- With respect to the charging experiment of the HT (Figure 13b), the highest $\Delta T_{Err,i}$ values are achieved at the IHX_HT outlet (fluctuating from a lowest value of -0.12 °C up to a maximum value of 0.12 °C). The values of $\Delta T_{Err,i}$ for nodes 1, 2, and 4 are equal to about 0.04 °C at the beginning and then keep within the range -0.02 °C ÷ 0.02 °C.
- For the discharging experiment of the HT (Figure 13c), the values of $\Delta T_{Err,i}$ for nodes 1, 2, 3, and 4 and the outlet of the HT are in the range of -0.07 °C ÷ -0.01 °C at the beginning and then remain between -0.02 °C and 0.02 °C.

- With respect to the simultaneous discharging/charging experiment of the HT (Figure 13d), the highest $\Delta T_{Err,i}$ values are recorded for node 3 and the IHX_HT outlet (ranging between a lowest value of −0.07 °C up to a maximum value of 0.09 °C); the values of $\Delta T_{Err,i}$ are equal to about −0.03 °C at the beginning and then remain within the range −0.01 °C ÷ 0.01 °C for nodes 1, 2, and 4 and the outlet of the HT.
- During the heat-up experiment of the CT (Figure 14a), $\Delta T_{Err,i}$ for nodes 1, 2, 3, and 4 keep within the range −0.02 °C ÷ 0.02 °C for the majority of the experiment, then they drop down to about 0.1 °C at the end of the experiment.
- For the charging experiment of the CT (Figure 14b), the highest $\Delta T_{Err,i}$ values are recorded at the IHX_CT outlet, with a minimum value of around −0.1 °C and a maximum value of around 0.06 °C. The data of $\Delta T_{Err,i}$ for the nodes 1, 2, and 4 stay within the range −0.02 °C ÷ 0.02 °C.
- With respect to the discharging experiment of the CT (Figure 14c), the values of $\Delta T_{Err,i}$ begin with values around 0.03 °C in the case of nodes 1, 2, 3, and 4 and the tank outlet; then, they all continue fluctuating between −0.015 °C and 0.015 °C.
- During the simultaneous discharging/charging experiment of the CT (Figure 14d), the highest $\Delta T_{Err,i}$ values are obtained at the IHX_CT outlet, with data ranging from the lowest value of −0.08 °C up to the highest value of 0.04 °C. $\Delta T_{Err,i}$ values vary between −0.01 °C and 0.01 °C for the majority of the test for nodes 1 and 4 and the tank outlet.

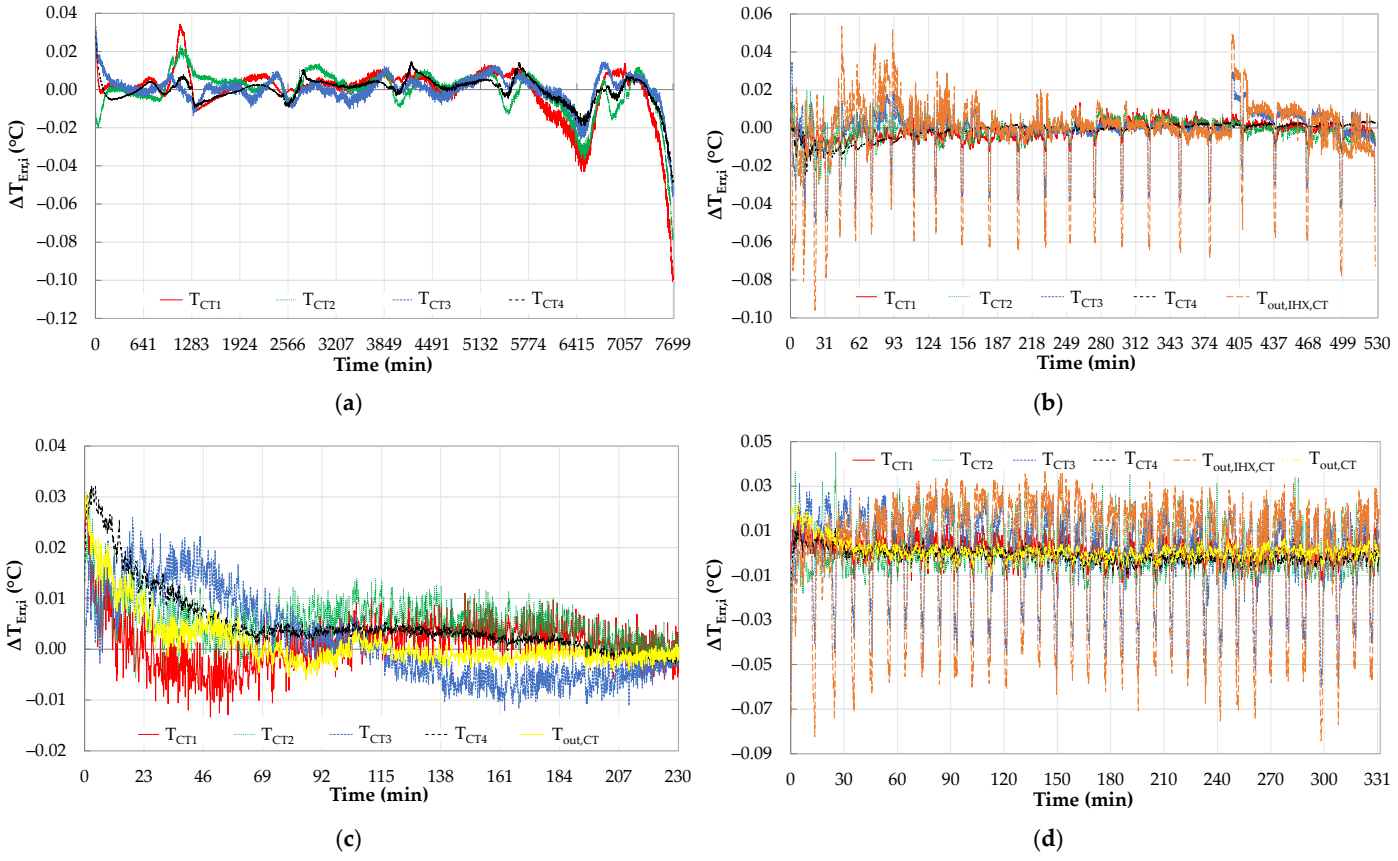


Figure 14. Values of $\Delta T_{Err,i}$ for ANN5 upon varying the time during the training experiments for the CT: (**a**) heat-up experiment, (**b**) charging experiment, (**c**) discharging experiment, (**d**) simultaneous discharging/charging experiment.

To better characterize the differences between the predictions of ANN5 and the experimental measurements for each experiment, the metrics defined by Equations (3)–(8) have been calculated. Tables A4 and A5 in Appendix A report the values of the above-mentioned

metrics upon varying the type of experiment for the HT and the CT, respectively. The blank cells in these tables correspond to the physically irrelevant measurements at each individual experiment. For example, there is no flow through IHX nor through the tank outlet in the cooldown experiment of the HT nor in the heat-up experiment of the CT; therefore, the parameters $T_{out,IHX,HT}$, $T_{out,HT}$, $T_{out,IHX,CT}$, and $T_{out,CT}$ have no physical meaning in these two experiments. The green shading in these tables has been given to the cells associated with the best performance for each line, while the red shading has been assigned to the worst performances. The main outcomes of Tables A4 and A5 can be summarized as follows:

- For the HT, the AE values range between $-78{\cdot}10^{-4}$ °C at node 2 during the HT discharging experiment to $52{\cdot}10^{-4}$ at node 2 throughout the HT charging experiment. The best values are $-2{\cdot}10^{-4}$ °C and $2{\cdot}10^{-4}$ °C, associated with the tank outlet and node 2, respectively, both recorded throughout the HT simultaneous discharging/charging experiment. With reference to the CT, the values of AE range between $-16{\cdot}10^{-4}$ °C (at node 1 and the IHX outlet through the charging experiment) and $55{\cdot}10^{-4}$ °C (at node 2 throughout the discharging experiment); the most accurate prediction (AE = 0 °C) is observed at node 3 during the simultaneous discharging/charging experiment.
- The lowest ABE for the HT is $3{\cdot}10^{-3}$ °C at node 2 during the simultaneous discharging/charging experiment, while the highest ABE is $45{\cdot}10^{-3}$ °C at the IHX outlet during the same experiment (Table A4). In the case of the CT, ABE values range from $2{\cdot}10^{-3}$ °C at node 4 to $21{\cdot}10^{-3}$ °C at the IHX outlet, both recorded during the simultaneous discharging/charging experiment (Table A5).
- For the HT, the lowest MSE is $1{\cdot}10^{-5}$ °C^2, achieved at node 2 throughout the simultaneous discharging/charging experiment, while the maximum MSE is $629{\cdot}10^{-5}$ °C^2, recorded at the IHX outlet throughout the charging experiment (Table A4). With reference to the CT, MSE values vary from $1{\cdot}10^{-5}$ °C^2 at node 4 throughout the simultaneous discharging/charging experiment to $71{\cdot}10^{-5}$ °C^2 at the IHX outlet throughout the same experiment (Table A5).
- The HT shows a minimum RMSE of $4{\cdot}10^{-3}$ °C at node 2 throughout the simultaneous discharging/charging experiment, and a maximum RMSE of $79{\cdot}10^{-3}$ °C at the IHX outlet throughout the charging experiment (Table A4). For the CT, RMSE ranges from $3{\cdot}10^{-3}$ °C at node 4 to $27{\cdot}10^{-3}$ °C at the IHX outlet, both corresponding to the simultaneous discharging/charging experiment (Table A5).
- With reference to the HT, the NRMSE lowest value of $3{\cdot}10^{-4}$ occurs at nodes 1–4 during the cooldown experiment, while the peak of $220{\cdot}10^{-4}$ corresponds to the IHX outlet throughout the simultaneous discharging/charging experiment (Table A4). In the case of the CT, NRMSE ranges from a minimum of $4{\cdot}10^{-4}$ at node 4 throughout the charging experiment to a maximum of $112{\cdot}10^{-4}$ at the IHX outlet throughout the simultaneous discharging/charging experiment (Table A5).
- According to Tables A4 and A5, the values of R^2 are always larger than 0.9900936. The lowest R^2 values are observed for both the HT and CT during the simultaneous discharging/charging experiment.

The values reported in Tables A4 and A5 indicate that there is an excellent match between the ANN5 predictions and the measured values, confirming the accuracy of the proposed model and its capability in accurately predicting the temperature trends at the six thermometers' locations across all experiments for both the CT and HT. These results are consistent also with the findings of Soomro et al. [44] indicating a lowest MSE of 0.03 °C^2 and a greatest R^2 of 0.92.

Moreover, the outputs predicted by the ANN5 model have also been contrasted with the experimental data measured during the experiments described in Section 3 terms of energy exchanged for both the HT and CT. In particular, (i) the predicted ($E_{Nc,HT,ANN}$) and measured ($E_{Nc,HT,Exp}$) energy exchanged throughout the natural cooldown experiment of the HT, (ii) the predicted ($E_{Ch,HT,ANN}$) and measured ($E_{Ch,HT,Exp}$) energy charged into the HT during the charging experiment, (iii) the predicted ($E_{Dis,HT,ANN}$) and measured ($E_{Dis,HT,Exp}$) energy discharged from the HT throughout the discharging experiment, (iv) the predicted ($E_{Nh,CT,ANN}$) and measured ($E_{Nh,CT,Exp}$) energy exchanged throughout the natural heat-up experiment of the CT, (v) the predicted ($E_{Ch,CT,ANN}$) and measured ($E_{Ch,CT,Exp}$) energy charged into the CT during the charging experiment, and (vi) the predicted ($E_{Dis,CT,ANN}$) and measured ($E_{Dis,CT,Exp}$) energy discharged from the CT during the discharging experiment have been calculated as follows:

$$E_{Nc,HT,ANN} = \rho \cdot c_p \cdot V_{tank} \cdot (\overline{T}_{HT,t_0} - \overline{T}_{HT,t_f,ANN}) \quad (9)$$

$$E_{Nc,HT,Exp} = \rho \cdot c_p \cdot V_{tank} \cdot (\overline{T}_{HT,t_0} - \overline{T}_{HT,t_f}) \quad (10)$$

$$E_{Ch,HT,ANN} = \int_{t_0}^{t_f} P_{Ch,HT,ANN} dt = \int_{t_0}^{t_f} \rho \cdot c_p \cdot V_{in,IHX,HT} \cdot (T_{in,IHX,HT} - T_{out,IHX,HT,ANN}) dt \quad (11)$$

$$E_{Ch,HT,Exp} = \int_{t_0}^{t_f} P_{Ch,HT,Exp} dt = \int_{t_0}^{t_f} \rho \cdot c_p \cdot V_{in,IHX,HT} \cdot (T_{in,IHX,HT} - T_{out,IHX,HT}) dt \quad (12)$$

$$E_{Dis,HT,ANN} = \int_{t_0}^{t_f} P_{Dis,HT,ANN} dt = \int_{t_0}^{t_f} \rho \cdot c_p \cdot V_{in,FC} \cdot (T_{out,HT,ANN} - T_{in,HT}) dt \quad (13)$$

$$E_{Dis,HT,Exp} = \int_{t_0}^{t_f} P_{Dis,HT,Exp} dt = \int_{t_0}^{t_f} \rho \cdot c_p \cdot V_{in,FC} \cdot (T_{out,HT} - T_{in,HT}) dt \quad (14)$$

$$E_{Nh,CT,ANN} = \rho \cdot c_p \cdot V_{tank} \cdot (\overline{T}_{CT,t_f,ANN} - \overline{T}_{CT,t_0}) \quad (15)$$

$$E_{Nh,CT,Exp} = \rho \cdot c_p \cdot V_{tank} \cdot (\overline{T}_{CT,t_f} - \overline{T}_{CT,t_0}) \quad (16)$$

$$E_{Ch,CT,ANN} = \int_{t_0}^{t_f} P_{Ch,CT,ANN} dt = \int_{t_0}^{t_f} \rho \cdot c_p \cdot V_{in,IHX,CT} \cdot (T_{out,IHX,CT,ANN} - T_{in,IHX,CT}) dt \quad (17)$$

$$E_{Ch,CT,Exp} = \int_{t_0}^{t_f} P_{Ch,CT,Exp} dt = \int_{t_0}^{t_f} \rho \cdot c_p \cdot V_{in,IHX,CT} \cdot (T_{out,IHX,CT} - T_{in,IHX,CT}) dt \quad (18)$$

$$E_{Dis,CT,ANN} = \int_{t_0}^{t_f} P_{Dis,CT,ANN} dt = \int_{t_0}^{t_f} \rho \cdot c_p \cdot V_{in,FC} \cdot (T_{in,CT} - T_{out,CT,ANN}) dt \quad (19)$$

$$E_{Dis,CT,Exp} = \int_{t_0}^{t_f} P_{Dis,CT,Exp} dt = \int_{t_0}^{t_f} \rho \cdot c_p \cdot V_{in,FC} \cdot (T_{in,CT} - T_{out,CT}) dt \quad (20)$$

where V_{tank} is the tank volume, $P_{Ch,HT,ANN}$ is the predicted thermal power charged into the HT, $P_{Ch,HT,Exp}$ is the measured thermal power charged into the HT, $P_{Dis,HT,ANN}$ is the predicted thermal power discharged from the HT, $P_{Dis,HT,Exp}$ is the measured thermal power discharged from the HT, $P_{Ch,CT,ANN}$ is the predicted cooling power charged into the CT, $P_{Ch,CT,Exp}$ is the measured cooling power charged into the CT, $P_{Dis,CT,ANN}$ is the predicted cooling power discharged from the CT, $P_{Dis,CT,Exp}$ is the measured cooling power discharged from the CT, ρ and c_p are, respectively, the density and the specific heat of the HCF, the values of $V_{in,FC}$, $V_{in,IHX,HT}$, $V_{in,IHX,CT}$, $T_{in,HT}$, $T_{out,HT}$, $T_{in,IHX,HT}$, $T_{out,IHX,HT}$, $T_{in,CT}$, $T_{out,CT}$, $T_{in,IHX,CT}$, and $T_{out,IHX,CT}$ are derived during the tests, t_0 and t_f are, respectively, the first and last time steps of the experiments, $\overline{T}_{HT,t_0}$ and $\overline{T}_{HT,t_f}$ are the arithmetic averages of the temperatures measured by the four sensors installed in the hot tank at the initial (t_0) and final (t_f) time steps, respectively, and $\overline{T}_{CT,t_0}$ and $\overline{T}_{CT,t_f}$ are the arithmetic averages of the temperatures measured by the four sensors installed in the cold tank at the initial (t_0) and final (t_f) time steps, respectively. $\overline{T}_{HT,t_f,ANN}$ and $\overline{T}_{CT,t_f,ANN}$ are the arithmetic

averages of the temperatures predicted by the ANN5-based model at nodes 1, 2, 3, and 4 of the hot tank and the cold tank, respectively, at the final time step (t_f), $T_{out,HT,ANN}$ and $T_{out,IHX,HT,ANN}$ are, respectively, the temperatures predicted by the ANN5-based model at the HT outlet and the IHX_HT outlet, and $T_{out,CT,ANN}$ and $T_{out,IHX,CT,ANN}$ are, respectively, the temperatures predicted by the ANN5-based model at the CT outlet and the IHX_CT outlet. The values of density and specific heat of the HCF were determined using data from the 2005 ASHRAE Handbook [45] according to the ethylene glycol concentration (that was measured and assumed equal to 6% by volume). Average values of these thermophysical properties over selected temperature intervals were adopted in this study in order to simplify the calculation by taking into account that their variability with temperature is reduced. Specifically, based on the operating scenarios of the experimental tests, the temperature range of 20 ÷ 50 °C is used to calculate the average density and specific heat of the heat carrier fluid in the HT, while the temperature range of 5 ÷ 25 °C is considered for the cold tank to derive the average density and specific heat of the heat carrier fluid in the case of the CT. In greater detail, c_p and ρ were assumed equal to 4.071 kJ/kgK and 1002.1 kg/m^3, respectively, for the HT, while c_p and ρ were considered equal to 4.054 kJ/kgK and 1008.4 kg/m^3 in the case of the CT.

According to Equations (9)–(20), a comparison between experimental and predicted data has been conducted by using the following metrics:

$$E_{Nc,HT,Err} = \frac{(E_{Nc,HT,ANN} - E_{Nc,HT,Exp})}{E_{Nc,HT,ANN}} \cdot 100\% \quad (21)$$

$$E_{Ch,HT,Err} = \frac{\left(E_{Ch,HT,ANN} - E_{Ch,HT,Exp}\right)}{E_{Ch,HT,ANN}} \cdot 100\% \quad (22)$$

$$E_{Dis,HT,Err} = \frac{(E_{Dis,HT,ANN} - E_{Dis,HT,Exp})}{E_{Dis,HT,ANN}} \cdot 100\% \quad (23)$$

$$E_{Nh,CT,Err} = \frac{\left(E_{Nh,CT,ANN} - E_{Nh,CT,Exp}\right)}{E_{Nh,CT,ANN}} \cdot 100\% \quad (24)$$

$$E_{Ch,CT,Err} = \frac{\left(E_{Ch,CT,ANN} - E_{Ch,CT,Exp}\right)}{E_{Ch,CT,ANN}} \cdot 100\% \quad (25)$$

$$E_{Dis,CT,Err} = \frac{(E_{Dis,CT,ANN} - E_{Dis,CT,Exp})}{E_{Dis,CT,ANN}} \cdot 100\% \quad (26)$$

Table 5 presents the metrics calculated via Equations (21)–(23) for the hot tank, while Table 6 indicates the metrics derived through Equations (24)–(26) for the CT. Due to the nature of the experiments conducted in this study, it is not possible to calculate the above metrics for all phases of the verification experiments.

Table 5. Comparison between predicted (by the ANN5 model) and measured energy values upon varying the phases of the experimental verification test for the HT.

Metrics	Cooldown Phase	Charging Phase	Discharging Phase	Simultaneous Discharging/Charging Phase
$E_{Nc,HT,Err}$ (%)	−0.122	Not applicable	Not applicable	Not applicable
$E_{Ch,HT,Err}$ (%)	Not applicable	−0.877	Not applicable	0.028
$E_{Dis,HT,Err}$ (%)	Not applicable	Not applicable	−0.835	−0.006

Table 6. Comparison between predicted (by the ANN5 model) and measured energy values upon varying the phases of the experimental verification test for the CT.

Metrics	Heat-Up Phase	Charging Phase	Discharging Phase	Simultaneous Discharging/Charging Phase
$E_{Nh,CT,Err}$ (%)	−0.890	Not applicable	Not applicable	Not applicable
$E_{Ch,CT,Err}$ (%)	Not applicable	−0.808	Not applicable	0.102
$E_{Dis,CT,Err}$ (%)	Not applicable	Not applicable	−0.364	−0.080

According to Table 5, the percentage differences range from a minimum of −0.877% (observed over the charging experiment of the HT) up to a maximum of 0.028% (corresponding to the charging phase of the simultaneous discharging/charging experiment of the HT). Similarly, with reference to Table 6, the percentage differences range between −0.890% (observed during the natural heat-up of the CT) and 0.102% (recognized during the charging phase of the simultaneous discharging/charging experiment of the CT). These results highlight the accuracy of the developed ANN5 model in predicting the real-world performance of the STES, regardless of which tank is being tested and under various boundaries. The findings of this study indicate that the discrepancies between the predicted and experimentally obtained energies are comparable with those indicated by Soomro et al. [44].

In order to complete the comparison between experimental and predicted data, the uncertainty related to the measured values has been determined for every time step, except in the case of the natural cooldown of the HT and heat-up of the CT where it has been calculated only once. Let us consider a measurand Y depending on a number of inputs $X_1, \ldots, X_N$ and let $x_1, \ldots, x_N$ be the measured values of $X_1, \ldots, X_N$, respectively. Substituting $x_1, \ldots, x_N$, to $X_1, \ldots, X_N$, respectively, it is possible to obtain an estimation y of the measurand Y. According to Moffat et al. [46], the absolute measurement error δy associated with y can be calculated as the root-sum squared combination of the absolute measurement errors $\delta x_1, \ldots, \delta x_N$ associated with the evaluation of $x_1, \ldots, x_N$, if $\delta x_1, \ldots, \delta x_N$ are independent and causal. In this study, the absolute measurement uncertainty $\delta E_{Nc,HT,Exp}$, $\delta P_{Ch,HT,Exp}$, $\delta P_{Dis,HT,Exp}$, $\delta E_{Nh,CT,Exp}$, $\delta P_{Ch,CT,Exp}$, $\delta P_{Dis,HT,Exp}$, and $\delta P_{Dis,CT,Exp}$ associated with the calculation of $E_{Nc,HT,Exp}$, $P_{Ch,HT,Exp}$, $P_{Dis,HT,Exp}$, $E_{Nh,CT,Exp}$, $P_{Ch,CT,Exp}$, and $\delta P_{Dis,CT,Exp}$ can be calculated according to the uncertainty analysis suggested by Mastrullo et al. [47] by using the subsequent formulas for the propagation of errors:

$$\delta E_{Nc,HT,Exp} = \rho \cdot V_{tank} \cdot c_p \cdot \sqrt{\left(\delta \overline{T}_{HT,t_0}\right)^2 + \left(\delta \overline{T}_{HT,t_f}\right)^2} \quad (27)$$

$$\delta P_{Ch,HT,Exp} = \rho \cdot c_p \cdot \sqrt{\left[\left(T_{in,IHX,HT} - T_{out,IHX,HT}\right) \cdot \delta V_{in,IHX}\right]^2 + \left(V_{in,IHX,HT} \cdot \delta T_{in,IHX,HT}\right)^2 + \left(V_{in,IHX} \cdot \delta T_{out,IHX,HT}\right)^2} \quad (28)$$

$$\delta P_{Dis,HT,Exp} = \rho \cdot c_p \cdot \sqrt{\left[\left(T_{out,HT} - T_{in,HT}\right) \cdot \delta V_{in,FC}\right]^2 + \left(V_{in,FC} \cdot \delta T_{in,HT}\right)^2 + \left(V_{in,FC} \cdot \delta T_{out,HT}\right)^2} \quad (29)$$

$$\delta E_{Nh,CT,Exp} = \rho \cdot V_{tank} \cdot c_p \cdot \sqrt{\left(\delta \overline{T}_{CT,t_0}\right)^2 + \left(\delta \overline{T}_{CT,t_f}\right)^2} \quad (30)$$

$$\delta P_{Ch,CT,Exp} = \rho \cdot c_p \cdot \sqrt{\left[\left(T_{out,IHX,CT} - T_{in,IHX,CT}\right) \cdot \delta V_{in,IHX,CT}\right]^2 + \left(V_{in,IHX,CT} \cdot \delta T_{in,IHX,CT}\right)^2 + \left(V_{in,IHX,CT} \cdot \delta T_{out,IHX,CT}\right)^2} \quad (31)$$

$$\delta P_{Dis,CT,Exp} = \rho \cdot c_p \cdot \sqrt{\left[\left(T_{in,CT} - T_{out,CT}\right) \cdot \delta V_{in,FC}\right]^2 + \left(V_{in,FC} \cdot \delta T_{in,CT}\right)^2 + \left(V_{in,FC} \cdot \delta T_{out,CT}\right)^2} \quad (32)$$

where $\delta V_{in,IHX,HT}$, $\delta V_{in,IHX,CT}$, $\delta V_{in,FC}$, $\delta \overline{T}_{HT,t_0}$, $\delta \overline{T}_{HT,t_f}$, $\delta T_{out,IHX,HT}$, $\delta T_{in,IHX,HT}$, $\delta T_{out,HT}$, $\delta T_{in,HT}$, $\delta \overline{T}_{CT,t_0}$, $\delta \overline{T}_{CT,t_f}$, $\delta T_{out,IHX,CT}$, $\delta T_{in,IHX,CT}$, $\delta T_{out,CT}$, and $\delta T_{in,CT}$ are the absolute measurement uncertainty of $V_{in,IHX,HT}$, $V_{in,IHX,CT}$, $V_{in,FC}$, $\overline{T}_{HT,t_0}$, $\overline{T}_{HT,t_f}$, $T_{out,IHX,HT}$, $T_{in,IHX,HT}$, $T_{out,HT}$, $T_{in,HT}$, $\overline{T}_{CT,t_0}$, $\overline{T}_{CT,t_f}$, $T_{out,IHX,CT}$, $T_{in,IHX,CT}$, $T_{out,CT}$, and $T_{in,CT}$, respectively (all these parameters are presented in Table 1). Based on Equations (27)–(32), it is feasible to compute the relative measurement uncertainty $\delta E_{Nc,HT,Exp}/E_{Nc,HT,Exp}$ associated with $E_{Nc,HT,Exp}$,

the relative measurement uncertainty $\delta P_{Ch,HT,Exp}/P_{Ch,HT,Exp}$ associated with $P_{Ch,HT,Exp}$, the relative measurement uncertainty $\delta P_{Dis,HT,Exp}/P_{Dis,HT,Exp}$ corresponding to $P_{Dis,HT,Exp}$, the relative measurement uncertainty $\delta E_{Nh,CT,Exp}/E_{Nh,CT,Exp}$ of $E_{Nh,CT,Exp}$, the relative measurement uncertainty $\delta P_{Ch,CT,Exp}/P_{Ch,CT,Exp}$ associated with $P_{Ch,CT,Exp}$, and the relative measurement uncertainty $\delta P_{Dis,CT,Exp}/P_{Dis,CT,Exp}$ corresponding to $P_{Dis,CT,Exp}$. The uncertainty assessment shows the following:

- The natural cooldown experiment of the HT, is characterized by a very low relative measurement uncertainty, approximately 0.220% of the experimental values of $E_{Nc,HT,Exp}$;
- Through the charging experiment of the HT, approximately 62% of the measured data of $P_{Ch,HT,Exp}$ obtained a relative measurement uncertainty smaller than 10%, while around 79% of the data regarding $P_{Ch,HT,Exp}$ are distinguished by a relative measurement uncertainty below 16%;
- Throughout the discharging experiment of the HT, around 53% of the measured data of $P_{Dis,HT,Exp}$ are marked by a relative measurement uncertainty smaller than 8%, while around 93% of the experimental data of $P_{Dis,HT,Exp}$ showed a relative measurement uncertainty smaller than 14%;
- Through the simultaneous discharging/charging experiment of the HT, almost 100% of the recorded data of $P_{Ch,HT,Exp}$ indicate a relative measurement uncertainty smaller than 4%, while around 99.98% of the of the recorded values of $P_{Dis,HT,Exp}$ are characterized by a relative measurement uncertainty less than 2%;
- The natural cooldown experiment of the CT is marked by a very low relative measurement uncertainty, approximately 0.388% of the recorded values of $E_{Nh,CT,Exp}$;
- Throughout the charging experiment of the CT, approximately 71% of the test data of $P_{Ch,CT,Exp}$ are distinguished by a relative measurement uncertainty less than 10%, while around 86% of the experimental data of $P_{Ch,CT,Exp}$ show a relative measurement uncertainty beneath 14%;
- Throughout the discharging experiment of the CT, around 52% of the measured datapoints of $P_{Dis,CT,Exp}$ have a relative measurement uncertainty smaller than 8%, while around 92% of the recorded data of $P_{Dis,CT,Exp}$ reveal a relative measurement uncertainty smaller than 14%;
- During the simultaneous discharging/charging experiment of the CT, almost 97% of the recorded data of $P_{Ch,CT,Exp}$ display a relative measurement uncertainty under 8%, while almost 100% of the experimental data of $P_{Dis,CT,Exp}$ report a relative measurement uncertainty less than 4%.

The arithmetic mean of relative uncertainties have been calculated for all experiments and the related findings can be summarized as follows:

- Arithmetic mean of relative measurement uncertainty equal to 9.02% with respect to $P_{Ch,HT,Exp}$ through the charging experiment of the HT;
- Arithmetic mean of relative measurement uncertainty equal to 7.53% with respect to $P_{Dis,HT,Exp}$ over the discharging experiment of the HT;
- Arithmetic mean of relative measurement uncertainty equal to 2.76% and 1.77%, respectively, with respect to $P_{Ch,HT,Exp}$ and $P_{Dis,HT,Exp}$ recorded through the simultaneous discharging/charging experiment of the HT;
- Arithmetic mean of relative measurement uncertainty equal to 8.37% with respect to $P_{Ch,CT,Exp}$ measured throughout the charging experiment of the CT;
- Arithmetic mean of relative measurement uncertainty equal to 8.06% in the case of $P_{Dis,CT,Exp}$ corresponding to the discharging experiment of the CT;

- Arithmetic mean of relative measurement uncertainty equal to about 5.29% and 2.78%, respectively, regarding $P_{Ch,CT,Exp}$ and $P_{Dis,CT,Exp}$ measured during the simultaneous discharging/charging experiment of the CT.

The findings of the measurement uncertainty analysis highlight that the discrepancies between the predicted and measured values presented in Tables 5 and 6 are aligned with the relative measurement uncertainties related to the empirical values; this indicates that the accuracy of the suggested ANN-based model to forecast both the CT and HT performance is high.

5. Verification of the ANN5 Model

To ensure the reproducibility of the results, the ANN development tracked a structured workflow within the MATLAB platform. First, raw experimental data were organized into a combined block corresponding to the eight operational modes to maintain sequential integrity. The NARX architecture was then subjected to a parametric sensitivity analysis of 28 configurations (varying hidden neurons and delays). This systematic approach was used to ensure that the performance of the optimal model (ANN5) was robust and not overly sensitive to the initial random weight distribution. The network was trained using the Levenberg–Marquardt algorithm, with early stopping applied when validation MSE failed to improve for six consecutive epochs.

In this section, the developed ANN5 model has been compared with the verification database consisting of experimental measurements collected from two new experimental tests performed (in addition to the training database described in Section 4) in order to furthermore verify the model's predictive capability with respect to measured data not included in the datasets used for training, validating, and testing ANN5 itself. These additional experimental tests are described in Section 5.1, while Section 5.2 compares the ANN5 model predictions in contrast with the data recorded over these additional experiments. Table A6 in Appendix A summarizes the total duration, sampling interval, number of samples per operating mode, and the starting and ending day/time of each experiment for both the eight independent training tests (four performed with reference to the HT and four performed with reference to the CT), as well as the two independent verification tests (one performed with reference to the HT and one performed with reference to the CT).

5.1. Verification Database: Additional Independent Tests for the ANN5 Model Verification

Two additional verification experiments have been performed (one targeting the HT and one targeting the CT) from 9:00 a.m. to 6:00 p.m. During the verification experiment for the HT, the HT has been linked on one side to the HP through the IHX_HT and on the other side to the FC system via the tank's inlet and outlet. Table 7 reports detailed information regarding the two verification tests targeting the HT and the CT, including the starting date/time, the ending date/time, the total test duration, the number of recorded samples, and the corresponding sampling interval.

Table 7. Dataset summary of the two verification experiments for both STES tanks.

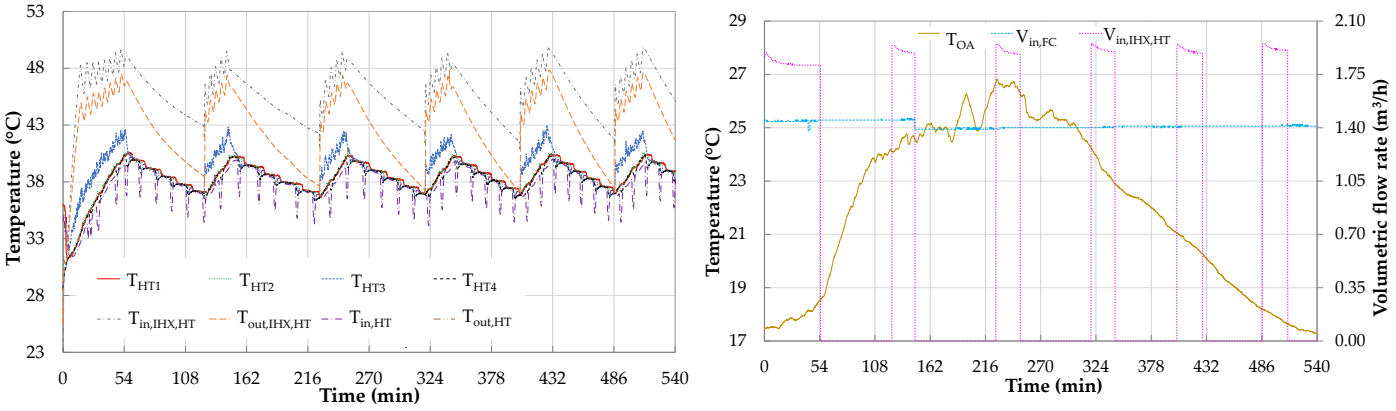
	Hot Tank	**Cold Tank**
Starting date (dd/mm/yyyy)	10/11/2022	15/11/2022
Starting time (hh:mm:ss)	09:00:00	09:00:00
Ending date (dd/mm/yyyy)	10/11/2022	15/11/2022
Ending time (hh:mm:ss)	18:00:00	18:00:00
Total duration (min)	540.0	540.0
Number of samples	6480	6480
Sampling interval (s)	5	5

The FC has been activated in order to keep a room temperature of 20 °C, with a dead band of ±0.2 °C; this means that when the room temperature rises to the upper limit of the dead band, the fan of the FC fan is switched off, but the HCF continues circulating through its heat exchanger; once the temperature becomes equal to the lower dead band limit, the FC fan is turned back on, while the HCF flow in the FC's heat exchanger is maintained. The stream between the HP and the IHX_HT has been managed in an on/off mode to keep the top node temperature of the HT within the range from 37 °C to 40 °C.

During the verification experiment for the CT, the CT has been linked on one side to the RS through the IHX_CT and on the other side to the FC through the tank's outlet and inlet. The FC has been controlled to keep a room temperature of 26 °C, with a dead band of ±0.2 °C. This means that when the room temperature drops to the lower limit of the dead band, the FC fan is turned off, but the HCF continues to flow through the FC's heat exchanger; once the room temperature achieves the upper limit of the dead band, the FC fan is reactivated, while the HCF continues to flow through its IHX. The stream between the RS and the IHX_CT has been managed in an on/off mode to keep the temperature at the lowest node of the CT between 13 °C and 16 °C.

Considering that both verification experiments have been performed during an intermediate season (i.e., fall), the heating, ventilation, and air-conditioning (HVAC) system which consists of a constant air volume dual-fan single-duct air-handling unit serving the SENS i-Lab test room has been utilized to artificially emulate the cooling and heating demands. Detailed information regarding the components and control logic of this HVAC system are reported in [48–50]. During the experiment focused on the HT, the HVAC system simulated the cooling demand by maintaining a setpoint room temperature of 18 °C, with a dead band of ±1 °C; conversely, during the test focused on the CT, the HVAC system simulated the heating demand by maintaining a setpoint temperature of 28 °C, with a dead band of ±1 °C.

Figure 15a shows the temporal trend of the measured HCF temperatures at the four HT nodes, as well as at the outlet and inlet of both the HT and the IHX_HT during the verification experiment related to the HT. Figure 15b reports the outside air temperature and the volumetric flowrates of the HCF flowing into the FC system and the IHX_HT upon varying the time during the same experiment.



(**a**) (**b**)

Figure 15. Measured data of HCF temperatures (T_{HT1}, T_{HT2}, T_{HT3}, T_{HT4}, $T_{in,IHX,HT}$, $T_{out,IHX,HT}$, $T_{in,HT}$, and $T_{out,HT}$) (**a**); volumetric flowrates ($V_{in,FC}$ and $V_{in,IHX,CT}$) of the HCF and temperature of outside air (T_{OA}) (**b**) upon varying the time through the verification experiment of the HT.

Similarly, Figure 16a displays the temporal trends of the measured HCF temperatures at the four CT nodes, along with the temperatures at the outlet and the inlet of both the CT and its IHX during the verification experiment of the CT. Figure 16b shows the outside

air temperature and the volumetric flowrates of the HCF entering the IHX_CT and the FC upon varying the time during the experiment.

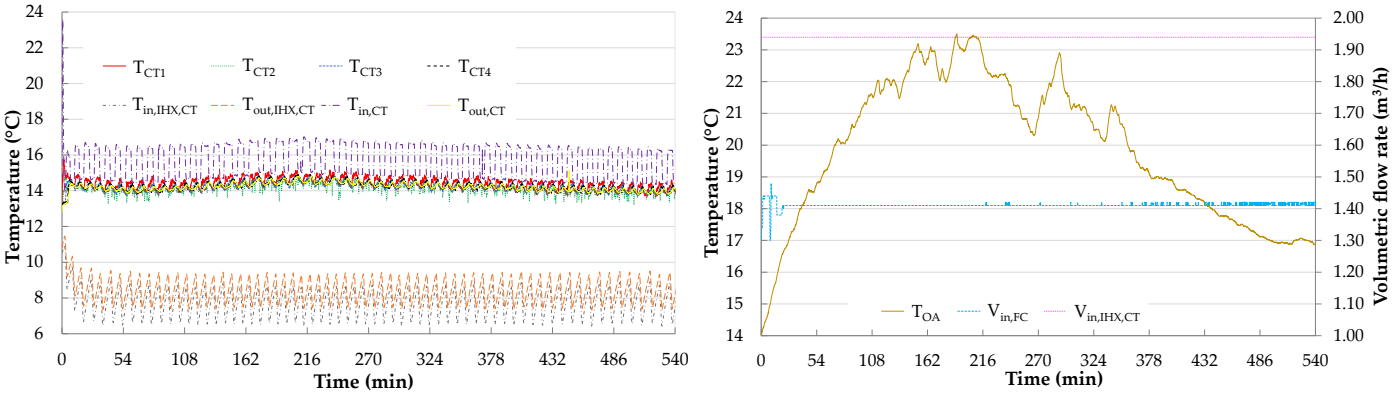


Figure 16. Measured data of HCF temperatures (T_{CT1}, T_{CT2}, T_{CT3}, T_{CT4}, $T_{in,IHX,CT}$, $T_{out,IHX,CT}$, $T_{in,CT}$, and $T_{out,CT}$) (**a**); volumetric flowrate ($V_{in,FC}$ and $V_{in,IHX,CT}$) of the HCF into the FC and temperature of outside air (T_{OA}) (**b**) upon varying the time during the verification experiment of the CT.

As illustrated in these figures, the flowrate of the HCF within the FC remains constant throughout both experiments, staying within the range between 1.40 m^3/h and 1.45 m^3/h.

More extensive information about the verification tests can be found in [33].

5.2. Independent Verification: Performance of ANN5 Model vs. The Experimental Verification Database

The ANN5 model was further validated using an independent dataset representing real-world operational scenarios, including simultaneous discharging/charging under heating and cooling modes. The ANN5-based model was converted to a closed-loop configuration for the independent verification against the tests in Section 5.1. Eleven parameters measured during the verification tests have been used as inputs for the ANN5 model. They consist of five predictors and six responses. The predictors are as follows: (1) temperature of the HCF at the inlet of the IHX measured at the previous time step (t − d); (2) volumetric flowrate of the HCF at the inlet of the IHX measured at the previous time step (t − d); (3) temperature of the HCF at the storage inlet measured at the previous time step (t − d); (4) volumetric flowrate of the HCF at the storage inlet measured at the previous time step (t − d); (5) outside air temperature measured at the previous time step (t − d). The responses are as follows: (1) temperature of the HCF at node 1 measured at the previous time step (t − d); (2) temperature of the HCF at node 2 measured at the previous time step (t − d); (3) temperature of the HCF at node 3 measured at the previous time step (t − d); (4) temperature of the HCF at node 4 measured at the previous time step (t − d); (5) temperature of the HCF at the IHX outlet measured at the previous time step (t − d); (6) temperature of the HCF at the storage inlet measured at the previous time step (t − d).

Figures 17 and 18 compare the measured temperatures in contrast with the predicted ones by the ANN5 model with reference to the verification test of the CT and the HT, respectively. Specifically, Figure 17 shows the values of $\Delta T_{Err,i}$ (Equation (2)) with reference to the temperature at the four nodes, the IHX exit, and the exit of the HT, while Figure 18 illustrates the values of $\Delta T_{Err,i}$ (Equation (2)) with reference to the temperature at the four nodes, the IHX exit, and the exit of the CT. Computing the values $\Delta T_{Err,i}$ is impossible when there is no flow in the IHX, so such periods are excluded from Figures 17 and 18. Figure 17 highlights that for the HT the values of $\Delta T_{Err,i}$ reach a maximum of 0.12 °C together with an average of −0.03 °C for T_{HT1}, a maximum of −0.17 °C together with

an average of −0.05 °C for T_{HT2}, and a maximum of 0.90 °C together with an average of 0.02 °C for T_{HT3}, a maximum of 0.14 °C together with an average of 0.01 °C for T_{HT4}. As for $T_{out,IHX,HT}$ and $T_{out,HT}$, their maximum $\Delta T_{Err,i}$ values are 1.87 °C and 0.12 °C, respectively, with average values of 0.07 °C and 0.0002 °C, respectively. Figure 18 indicates that for the CT the values of $\Delta T_{Err,i}$ achieve a maximum of −0.15 °C together with an average of −0.001 °C for T_{CT1}, a maximum of −0.16 °C together with an average of −0.004 °C for T_{CT2}, a maximum of 0.12 °C together with an average of 0.03 °C for T_{CT3}, and a maximum of −0.10 °C together with an average of 0.001 °C for T_{CT4}. As for $T_{out,IHX,CT}$ and $T_{out,CT}$, their maximum $\Delta T_{Err,i}$ values are −0.19 °C and −0.13 °C, respectively, with average values of 0.06 °C and −0.001 °C, respectively. Both Figures 17 and 18 clearly show that the predicted trends of the HCF temperatures at the distinct four nodes, the IHX outlet, and the tank outlet closely match the measured data for both cold and hot storage; this underlines that the proposed ANN5 model successfully captures the real-world performance of the tanks.

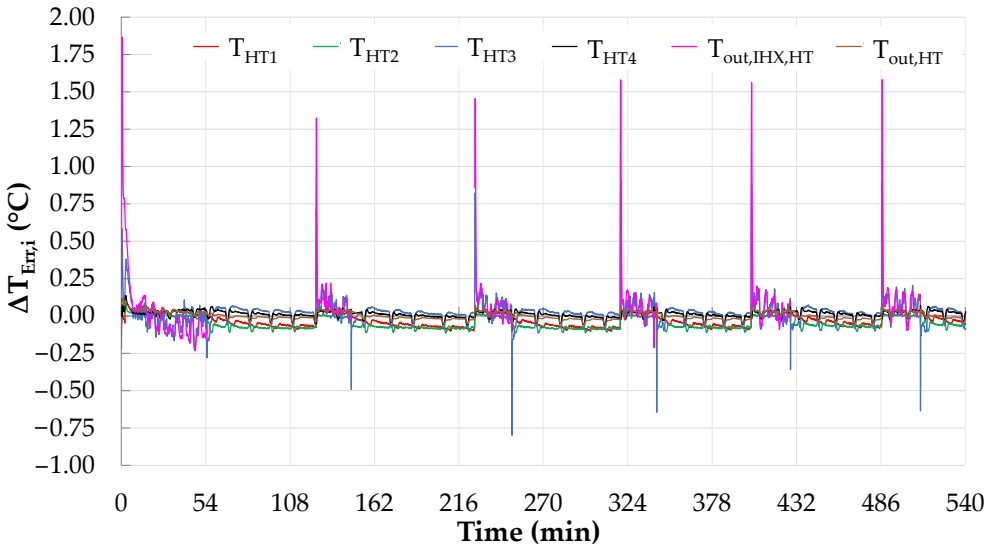


Figure 17. Values of $\Delta T_{Err,i}$ (Equation (2)) with reference to the temperature at the 4 nodes (T_{HT1}, T_{HT2}, T_{HT3}, and T_{HT4}), the IHX outlet ($T_{out,IHX,HT}$), and the outlet of the HT ($T_{out,HT}$).

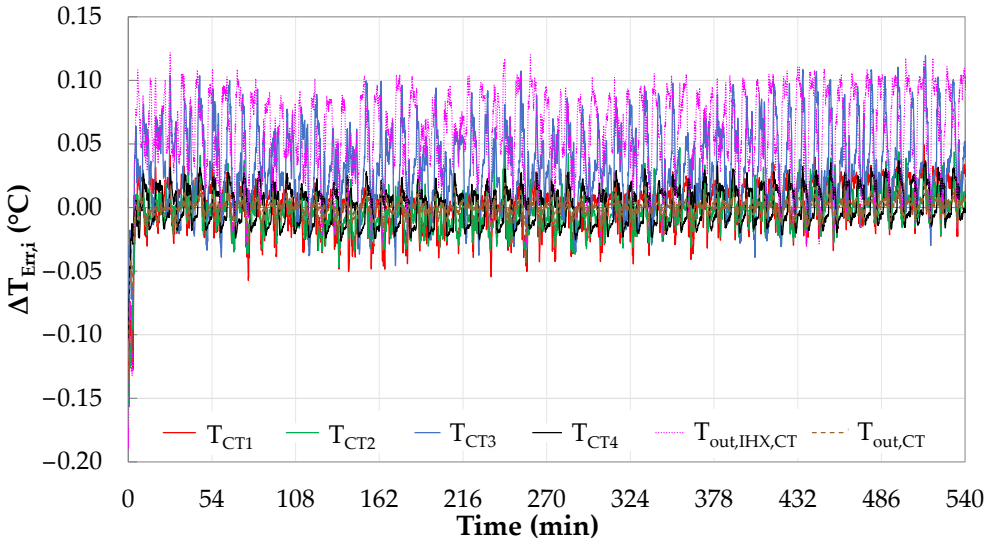


Figure 18. Values of $\Delta T_{Err,i}$ (Equation (2)) with reference to the temperature at the 4 nodes (T_{CT1}, T_{CT2}, T_{CT3}, and T_{CT4}), the IHX outlet ($T_{out,IHX,CT}$), and the outlet ($T_{out,CT}$) of the CT.

With reference to the values of $\Delta T_{Err,i}$ indicated in Figures 17 and 18, Table 8 reports the maximum $\Delta T_{Err,i}$, minimum $\Delta T_{Err,i}$, 95th percentile of positive $\Delta T_{Err,i}$ values, 95th

percentile of negative $\Delta T_{Err,i}$ values, and the time $T_{out,\pm 95th}$ with values of $\Delta T_{Err,i}$ larger than the 95th percentile of positive $\Delta T_{Err,i}$ values or lower than the 95th percentile of negative $\Delta T_{Err,i}$ values. These parameters are calculated with reference to all temperatures reported in Figures 17 and 18.

Table 8. Quantitative summary of $\Delta T_{Err,i}$ values as a function of the verification experiment and temperature levels.

		Maximum $\Delta T_{Err,i}$ (°C)	Minimum $\Delta T_{Err,i}$ (°C)	95th Percentile of Positive $\Delta T_{Err,i}$ (°C)	95th Percentile of Negative $\Delta T_{Err,i}$ (°C)	$T_{out,\pm 95th}$ (min)
Verification test of the HT	T_{HT1}	0.125	−0.106	0.058	−0.087	27.917
	T_{HT2}	0.088	−0.174	0.026	−0.099	27.917
	T_{HT3}	0.901	−0.799	0.139	−0.127	28.000
	T_{HT4}	0.137	−0.060	0.043	−0.048	27.917
	$T_{out,IHX,HT}$	1.866	−0.232	0.625	−0.151	8.833
	$T_{out,HT}$	0.120	−0.055	0.047	−0.042	28.000
Verification test of the CT	T_{CT1}	0.049	−0.148	0.028	−0.036	27.417
	T_{CT2}	0.048	−0.157	0.027	−0.029	27.333
	T_{CT3}	0.110	−0.094	0.085	−0.037	25.833
	T_{CT4}	0.037	−0.104	0.027	−0.022	27.333
	$T_{out,IHX,CT}$	0.122	−0.189	0.099	−0.113	24.083
	$T_{out,CT}$	0.021	−0.134	0.011	−0.015	27.333

This table underlines that for the HT verification test the largest $\Delta T_{Err,i}$ is 1.866 °C, while the smallest $\Delta T_{Err,i}$ is −0.799 °C. With reference to the CT validation test, the largest $\Delta T_{Err,i}$ is 0.122 °C, while the smallest $\Delta T_{Err,i}$ is −0.189 °C. The highest values of $T_{out,\pm 95th}$ are 28.000 min for the HT and 27.417 min for the CT.

Table 9 underlines the statistical metrics AE (Equation (3)), ABE (Equation (4)), MSE (Equation (5)), RMSE (Equation (6)), NRMSE (Equation (7)), and R^2 (Equation (8)) with reference to the temperature at the four nodes, the IHX outlet, and the tank outlet for both the CT and the HT. Table 9 shows that the AE values range between −0.0501 °C at node 2 of the HT and 0.0249 °C at node 3 of the HT. The best value is 0.0002 °C and it is associated with the HT outlet.

Table 9. Statistical comparison of temperatures for the verification experiments of both the HT and the CT for the ANN5 model.

	Hot Tank					
	AE (°C)	**ABE (°C)**	**MSE (°C²)**	**RMSE (°C)**	**NRMSE**	**R^2**
T_{HT1}	−0.0286	0.0462	0.0027	0.0521	0.0056	0.9988
T_{HT2}	−0.0501	0.0545	0.0040	0.0636	0.0060	0.9984
T_{HT3}	0.0249	0.0515	0.0073	0.0854	0.0059	0.9977
T_{HT4}	0.0126	0.0214	0.0007	0.0262	0.0022	0.9997
$T_{out,IHX,HT}$	0.0248	0.0502	0.0187	0.1368	0.0061	0.9981
$T_{out,HT}$	0.0002	0.0218	0.0007	0.0261	0.0027	0.9997
	Cold tank					
	AE (°C)	**ABE (°C)**	**MSE (°C²)**	**RMSE (°C)**	**NRMSE**	**R^2**
T_{CT1}	−0.0009	0.0144	0.0004	0.0204	0.0098	0.9953
T_{CT2}	−0.0039	0.0120	0.0003	0.0172	0.0102	0.9963
T_{CT3}	0.0336	0.0374	0.0020	0.0452	0.0283	0.9699
T_{CT4}	0.0012	0.0134	0.0002	0.0154	0.0094	0.9960
$T_{out,IHX,CT}$	0.0579	0.0609	0.0046	0.0678	0.0164	0.9888
$T_{out,CT}$	−0.0009	0.0052	0.0001	0.0091	0.0057	0.9984

With reference to the CT, the values of AE range between −0.0039 °C (at node 2) and 0.579 °C (at the IHX_CT outlet); the most accurate prediction (AE= −0.0009 °C) is observed at both node 1 and the CT outlet.

The values of ABE range between a lowest value of 0.0214 °C obtained at node 4 and a highest value of 0.0545 °C observed at node 2 of the HT, while it ranges between 0.0052 °C and 0.0609 °C at the CT exit and the IHX_CT exit, respectively.

The values of MSE vary from the lowest value of 0.0007 °C^2 at both the HT outlet and node 4 of the HT up to the highest value of 0.0187 °C^2 at the IHX_HT exit, while it changes between 0.0001 °C^2 and 0.0046 °C^2 at the CT exit and the IHX_CT exit, respectively.

The highest RMSE is 0.1368 °C at the IHX_HT, while the lowest RMSE is 0.0261 °C at the HT outlet; it varies from the least values of 0.0091 °C at the exit of the CT up to the greatest of 0.0678 °C at the IHX outlet of the CT.

The highest NRMSE is 0.0061 for the IHX_HT outlet, while the lowest NRMSE is 0.0022 for node 4 of the HT; it changes from the lowest value of 0.0057 for the outlet of the CT up to the highest value of 0.0283 at node 3 of the CT.

The values of R^2 range from the fewest value of 0.9977 for node 3 of the HT up to the greatest value of 0.9997 at node 4 and the HT outlet, while it falls within 0.9699 and 0.9984 for node 3 of the CT and the outlet of the CT, respectively.

Lee et al. [18] and Nash et al. [43] reported a minimum NRMSE value equal to 0.0021 and 0.045, respectively. Soomro et al. [44] reported a minimal value of MSE equal to 0.03 °C^2, as well as a maximum R^2 equal to 0.92. Additionally, Van Schalkwyk et al. [51] examined thermal stratification and energy distribution across various operational scenarios using an experimentally validated CFD model of a horizontally oriented electric hot-water storage cylinder with a resistive immersion heating coil. The CFD model demonstrated a RMSE of 1.5 °C when compared to experimental data, higher than the values obtained in this study which vary between 0.0091 °C and 0.1368 °C. Based on these results in the literature, it can be concluded that the ANN5 model proposed in this work is consistent with the outcomes of similar scientific papers and it is highly accurate in predicting the temperature trends at the tank outlets and the IHX outlets for both the HT and CT.

The predicted results derived based on the ANN5 model have also been contrasted with the experimental charging/discharging daily energies for both the CT and the HT via Equations (22), (23), (25), and (26). The parameters used in Equations (22), (23), (25), and (26) have been calculated via Equations (11)–(14) for the HT and via Equations (17)–(20) for the CT. Table 10 presents the above-mentioned metrics calculated according to Equations (22), (23), (25), and (26).

Table 10. Comparison of predicted and measured energy values related to the verification experiments of both the CT and the HT by using the ANN5 model.

$E_{Ch,HT,Err}$ (%)	$E_{Ch,CT,Err}$ (%)	$E_{Dis,HT,Err}$ (%)	$E_{Dis,CT,Err}$ (%)
−3.87	7.08	0.09	0.13

This table shows that the predicted result slightly underestimates the measured charging daily energy for the HT ($E_{Ch,HT,Exp}$) by −3.87%, while it overestimates the measured charging daily energy for the CT ($E_{Ch,CT,Exp}$) by 7.08%; the ANN5 model slightly overestimates the measured discharging daily energy for the HT ($E_{Dis,HT,Exp}$) and the CT ($E_{Dis,CT,Exp}$) by 0.09% and 0.13%, respectively. These small percentage differences, particularly in the case of measured discharging daily energy, highlight the accuracy of the ANN5 model in reflecting and representing the real-world performance of the STES. The results reported in Table 10 are in line with the findings reported in Scapino et al. [6], where a relative energy

error between −3% and 4.2% has been obtained when a neural network model has been used for modeling a thermal energy storage system.

The uncertainties $\delta P_{Ch,HT,Exp}$, $\delta P_{Ch,CT,Exp}$, $\delta P_{Dis,HT,Exp}$, and $\delta P_{Dis,CT,Exp}$ associated with the measured value of $P_{Ch,HT,Exp}$, $P_{Ch,CT,Exp}$, $P_{Dis,HT,Exp}$, and $P_{Dis,CT,Exp}$ have been calculated based on Equations (28), (29), (31), and (32), respectively. The measurement uncertainty analysis indicated the following:

- Around 98% of the experimental data of $P_{Ch,HT,Exp}$ are distinguished by a relative measurement uncertainty lower than 4% over the charging phases of the HT;
- Over than 99% of the experimental data of $P_{Ch,CT,Exp}$ exhibit a relative measurement uncertainty smaller than 6% during the phases of charging of the CT;
- Throughout the discharging phases of the HT, around 17% of the measured data of $P_{Dis,HT,Exp}$ achieve a relative measurement uncertainty smaller than 2%, while around 72% of the experimental data of $P_{Dis,HT,Exp}$ have a relative measurement uncertainty smaller than 10%;
- Throughout the discharging phase of the CT, around 51% of the measured data of $P_{Dis,CT,Exp}$ have a relative measurement uncertainty smaller than 2%, while about 87% of the measured data of $P_{Dis,CT,Exp}$ achieve a relative measurement uncertainty smaller than 10%.

The arithmetic means of the relative uncertainties are as follows:

- 2.79% with respect to $P_{Ch,HT,Exp}$ throughout the phases of charging of the HT;
- 4.18% with respect to $P_{Ch,CT,Exp}$ throughout the phases of charging of the CT;
- 7.69% with respect to $P_{Dis,HT,Exp}$ throughout the phases of discharging of the HT;
- 4.91% with respect to $P_{Dis,CT,Exp}$ throughout the phases of discharging of the CT.

The above-mentioned data highlight that the discrepancies between the predicted and measured values presented in Table 10 are aligned with the calculated relative measurement uncertainties. For example, the difference between the predicted and measured values of thermal energy exchanged in the verification tests during the charging phases is −3.87% and 7.08% (Table 10) for the HT and the CT, respectively, while the minimum relative uncertainty of thermal energy measured during the verification tests in the case of the charging phases is 2.86% and 0.82% for the HT and the CT, respectively. Furthermore, the difference between the predicted and measured values of thermal energy exchanged in the verification tests in the case of the discharging phases is 0.09% and 0.13% (Table 10) for the HT and the CT, respectively, while the minimum relative uncertainty of thermal energy measured during the verification tests in the case of the discharging phases is 0.48% and 1.34% for HT and CT, respectively. This underlines that the capability of the proposed ANN5 model in predicting the performances of both the HT and the CT is high. In addition, the results reported in Table 10 show that the differences between the predicted and measured values for the CT over the charging phase are greater than those associated with the HT; this result is also due to the fact that the uncertainties of measurements associated with the charging phase of the CT are often larger than those related to the HT.

The performance and associated errors of the ANN model offer direct physical insights into the system's operational dynamics [52]. Specifically, the model's largest deviations between predicted and measured temperature profiles occur during periods of high transient behavior (i.e., fluctuating radiation or flowrates). This behavior is fundamentally explained by two phenomena (thermal stratification and system energy storage dynamics). Stratification leads to nonlinear temperature distribution within the storage tank, introducing complexities that the network, to be maintained in the same form as already submitted. More critically, the consistent lag in the ANN's predicted temperature response compared to the experimental measurements confirms the significant influence of thermal inertia.

During system start-up or sudden radiation spikes, a measurable amount of energy is temporarily consumed to charge the storage mass, delaying the fluid's outlet temperature rise. The difference between the ANN-predicted responses and the measured outcomes is, therefore, a quantifiable representation of the energy absorbed by the system's thermal mass, directly linking the network's predictive limitations to fundamental heat transfer and energy storage principles. In greater detail, it can be noticed that during the verification tests the HCF moves through the tank at a volumetric flowrate of approximately 1.40 m^3/h; at this speed, the theoretical residence time, which is the time it takes for water to fully cycle through the tank, is about 12.8 min; in contrast, the ANN5 model updates its predictions every 5 s. Because the model's memory window is so much shorter than the theoretical residence time of the HCF, a natural thermal lag occurs during sudden transitions. The transient errors reported in Figures 17 and 18 are a measurement of this thermal inertia; they represent the time the 300 L volume needs to absorb or release energy before the outlet temperature can fully react.

Empirical findings from black-box approaches are often limited by the boundary conditions and parameter ranges, which can limit their general applicability; the model's reliability is highest when the inputs remain within the temperature and flowrate ranges. As a consequence, it should be underlined that the proposed ANN5-based model refers to the specific experimental setup explained in Section 2 and it can be applied with the above-mentioned accuracy to STESs characterized by similar geometry, instrumentation layout, operational flows and loads, climates and control modes associated with training and verification tests. The ANN5 model demonstrated a high degree of generalization and proved by its ability to accurately forecast system behavior during both training and verification tests (i.e., independent datasets). However, its transferability to different scenarios must be preliminarily and further verified after a minimum retraining based on related performance data.

6. Conclusions

This study presents a data-driven ANN model capable of accurately predicting the thermal behavior of short-term STES units under diverse operating conditions. Among the 28 tested architectures, ANN5 (12 neurons, delay = 1) achieved the best overall performance, with NRMSE values as low as 0.0022 and R^2 exceeding 0.9699 for most temperature predictions. The model demonstrated strong generalization capabilities by accurately reproducing experimental results from independent verification tests, including both heating and cooling operations. Furthermore, daily energy predictions exhibited minimal deviation from measured values, confirming the model's suitability for real-world applications.

Compared to physics-based and CFD models, the proposed ANN approach offers rapid computation and reduced complexity, making it ideal for integration into building energy management systems, predictive control strategies, and digital twin frameworks.

Our next research steps will be directed towards integrating the proposed ANN model with physics-based models of STESs, leading to a hybrid gray-box modeling framework that combines the predictive accuracy of data-driven approaches with the interpretability and generalizability of physical models. Such kinds of framework could help in accounting for tank volumes, geometries, and insulation properties varying with respect to those investigated in this study. The proposed model can also serve as a detailed tool for analyzing and optimizing the energy, environmental, and economic performance of STES-based energy systems as operating conditions vary. It can be embedded within smart building energy management systems to enable autonomous decision-making, predictive control, and adaptive scheduling. In addition, the developed ANN model can be potentially applied in system design optimization, predictive maintenance, or real-time control. In

particular, it can be used for real-time forecasting and control of thermal energy flows, which supports dynamic optimization of HVAC systems and enhances overall building energy efficiency; the ANN model is also compatible with IoT platforms and sensor networks (allowing seamless data acquisition and system responsiveness in smart environments) and, therefore, it could also serve as a digital twin for STES systems, enabling virtual testing, fault detection, and performance benchmarking.

Author Contributions: Conceptualization, A.R., A.A.-S. and M.G.G.; methodology, A.R., M.E.Y., A.C., H.D., A.A.-S. and M.G.G.; software, A.R., M.E.Y., A.C. and H.D.; validation, A.R., M.E.Y., A.C., H.D., A.A.-S. and M.G.G.; formal analysis, A.R., M.E.Y., A.C., H.D., A.A.-S. and M.G.G.; investigation, A.R., M.E.Y., A.C. and H.D.; resources, A.R.; data curation, A.R., M.E.Y., A.C. and H.D.; writing—original draft preparation, A.R., M.E.Y., A.C., H.D., A.A.-S. and M.G.G.; writing—review and editing, A.R., M.E.Y., A.C., H.D., A.A.-S. and M.G.G.; visualization, A.R., M.E.Y., A.C., H.D., A.A.-S. and M.G.G.; supervision, A.R., A.A.-S. and M.G.G.; project administration, A.R.; funding acquisition, A.R. All authors have read and agreed to the published version of the manuscript.

Funding: This research received no external funding.

Data Availability Statement: The materials and data that support the findings of this study are available from the authors.

Acknowledgments: This study has been performed as part of the research activities under the collaboration agreement between the Department of Mechanical Engineering of the National University College of Technology (Jordan) and the Department of Architecture and Industrial Design of the University of Campania Luigi Vanvitelli (Italy). This study has been also performed in the framework of the project titled "Sviluppo di Sistemi Energetici Resilienti e Intelligenti per Comunita Energetiche Rinnovabili Residenziali e Commerciali—SERIREC"—CUP: E63C22002160007, supported by the Italian Government PNRR Grant No. PE00000021—PNRR—Mission 4—Component 2—Investment 1.3—Funded by the European Union—NextGenerationEU—Ministerial Decree No. 341 dated 15 March 2022—Cascade Call for the Extended Partnership "NEST—Network 4 Energy Sustainable Transition" Spoke 7 "Smart Sector Integration"—Ministerial Decree No. 800 dated 24 June 2024.

Conflicts of Interest: The authors declare no conflicts of interest.

Abbreviations

The following abbreviations are used in this manuscript:

ABE	Average absolute error (°C)
AE	Average error (°C)
ANN	Artificial neural network
BiLSTM	Bidirectional long short-term memory
c_p	Specific heat (kJ/kgK)
CT	Cold tank
CFD	Computational fluid dynamics
CNN	Cascade correlation neural network
d	Delay
De	Outer diameter of tank (m)
$D_{out,IHX}$	Outer tube diameter of internal heat exchanger (mm)
$E_{Ch,CT,ANN}$	Predicted daily charged energy for cold tank (kJ)
$E_{Ch,CT,Exp}$	Measured daily charged energy for cold tank (kJ)
$E_{Ch,CT,Err}$	Difference between predicted and measured daily charged energy for cold tank (%)
$E_{Ch,HT,ANN}$	Predicted daily charged energy for hot tank (kJ)
$E_{Ch,HT,Exp}$	Measured daily charged energy for hot tank (kJ)

$E_{Ch,HT,Err}$	Difference between predicted and measured daily charged energy for hot tank (%)
$E_{Dis,CT,ANN}$	Predicted daily discharged energy for cold tank (kJ)
$E_{Dis,CT,Exp}$	Measured daily discharged energy for cold tank (kJ)
$E_{Dis,CT,Err}$	Difference between predicted and measured daily discharged energy for cold tank (%)
$E_{Dis,HT,ANN}$	Predicted daily discharged energy for hot tank (kJ)
$E_{Dis,HT,Exp}$	Measured daily discharged energy for hot tank (kJ)
$E_{Dis,HT,Err}$	Difference between predicted and measured daily discharged energy for hot tank (%)
$E_{Nc,HT,ANN}$	Predicted daily cooldown energy losses for hot tank (kJ)
$E_{Nc,HT,Exp}$	Measured daily cooldown energy losses for hot tank (kJ)
$E_{Nc,HT,Err}$	Difference between predicted and measured daily cooldown energy losses for hot tank (%)
$E_{Nh,CT,ANN}$	Predicted daily heat-up energy losses for cold tank (kJ)
$E_{Nh,CT,Exp}$	Measured daily heat-up energy losses for cold tank (kJ)
$E_{Nh,CT,Err}$	Difference between predicted and measured daily heat-up energy losses for cold tank (%)
FC	Fan coil
GRU	Gated recurrent unit
HCF	Heat carrier fluid
HP	Heat pump
HT	Hot tank
HVAC	Heating, ventilation, and air-conditioning
i	Time step (s)
ICT	Internal cold tank of refrigerating system
IHT	Internal hot tank of heat pump
IHX	Internal heat exchanger
IHX_CT	Internal heat exchanger inside cold tank
IHX_HT	Internal heat exchanger inside hot tank
LSTM	Long short-term memory
MSE	Mean square error ($°C^2$)
NARX	Nonlinear auto-regressive with exogenous inputs
NRMSE	Normalized root mean square error
$P_{Ch,CT,ANN}$	Predicted charged power for cold tank (W)
$P_{Ch,CT,Exp}$	Measured charged power for cold tank (W)
$P_{Ch,HT,ANN}$	Predicted charged power for hot tank (W)
$P_{Ch,HT,Exp}$	Measured charged power for hot tank (W)
$P_{Dis,CT,ANN}$	Predicted discharged power for cold tank (W)
$P_{Dis,CT,Exp}$	Measured discharged power for cold tank (W)
$P_{Dis,HT,ANN}$	Predicted discharged power for hot tank (W)
$P_{Dis,HT,Exp}$	Measured discharged power for hot tank (W)
R^2	Coefficient of determination
RMSE	Root mean square error (°C)
RS	Refrigerating system
STES	Sensible thermal energy storage
t	Time (s)
t_0	Initial experimental time (s)
t_f	Final experimental time (s)
$T_{ANN,i}$	Predicted temperature of a specific node at time step i (°C)
TCN	Temporal convolutional network
T_{CT1}	Temperature of heat carrier fluid at node 1 of cold tank (°C)
T_{CT2}	Temperature of heat carrier fluid at node 2 of cold tank (°C)
T_{CT3}	Temperature of heat carrier fluid at node 3 of cold tank (°C)

T_{CT4}	Temperature of heat carrier fluid at node 4 of cold tank (°C)
$T_{exp,i}$	Measured heat carrier fluid temperature of a specific node at time step i (°C)
$T_{exp,max}$	Maximum measured temperature (°C)
$T_{exp,min}$	Minimum measured temperature (°C)
$\overline{T}_{exp}$	Arithmetic mean of measured heat carrier fluid temperatures (°C)
T_{HT1}	Temperature of heat carrier fluid at node 1 of hot tank (°C)
T_{HT2}	Temperature of heat carrier fluid at node 2 of hot tank (°C)
T_{HT3}	Temperature of heat carrier fluid at node 3 of hot tank (°C)
T_{HT4}	Temperature of heat carrier fluid at node 4 of hot tank (°C)
$\overline{\overline{T}}_{CT,t_0}$	Arithmetic average of heat carrier fluid temperatures measured at four distinct heights inside cold tank at initial time t_0 (°C)
$\overline{\overline{T}}_{CT,t_f}$	Arithmetic average of heat carrier fluid temperatures measured at four distinct heights inside cold tank at final time t_f (°C)
$\overline{\overline{T}}_{HT,t_0}$	Arithmetic average of heat carrier fluid temperatures measured at four distinct heights inside hot tank at initial time t_0 (°C)
$\overline{\overline{T}}_{HT,t_f}$	Arithmetic average of heat carrier fluid temperatures measured at four distinct heights inside hot tank at final time t_f (°C)
$T_{in,CT}$	Temperature of heat carrier fluid at inlet of cold tank (°C)
$T_{in,FC}$	Temperature of heat carrier fluid at inlet of fan coil (°C)
$T_{in,HT}$	Temperature of heat carrier fluid at hot tank inlet (°C)
$T_{in,HP}$	Temperature of heat carrier fluid at inlet of heat pump (°C)
$T_{in,IHX}$	Temperature of heat carrier fluid at internal heat exchanger inlet of tank (°C)
$T_{in,IHX,CT}$	Temperature of heat carrier fluid at internal heat exchanger inlet of cold tank (°C)
$T_{in,IHX,HT}$	Temperature of heat carrier fluid at internal heat exchanger inlet of hot tank (°C)
$T_{in,RS}$	Temperature of heat carrier fluid at inlet of refrigerating system (°C)
T_{OA}	Temperature of outside air (°C)
$T_{out,CT}$	Temperature of heat carrier fluid at cold tank outlet (°C)
$T_{out,CT,ANN}$	Predicted heat carrier fluid temperature at cold tank outlet (°C)
$T_{out,FC}$	Temperature of heat carrier fluid at outlet of fan coil (°C)
$T_{out,HT}$	Temperature of heat carrier fluid at hot tank outlet (°C)
$T_{out,HP}$	Temperature of heat carrier fluid at outlet of heat pump (°C)
$T_{out,HT,ANN}$	Predicted temperature at hot tank outlet (°C)
$T_{out,IHX,CT}$	Temperature of heat carrier fluid at internal heat exchanger outlet of cold tank (°C)
$T_{out,IHX,CT,ANN}$	Predicted heat carrier fluid temperature at internal heat exchanger outlet of cold tank (°C)
$T_{out,IHX,HT}$	Temperature of heat carrier fluid at internal heat exchanger outlet of hot tank (°C)
$T_{out,IHX,HT,ANN}$	Predicted heat carrier fluid temperature at internal heat exchanger outlet of hot tank (°C)
$T_{out,RS}$	Temperature of heat carrier fluid at refrigerating system outlet (°C)
$T_{out,\pm 95th}$	Period with $\Delta T_{Err,i}$ larger than the 95th percentile of positive $\Delta T_{Err,i}$ values or lower than the 95th percentile of negative $\Delta T_{Err,i}$ values (min)
T_{Room}	Air temperature inside test room
T_{Room}	Air temperature inside test room (°C)
TES	Thermal energy storage
$V_{in,CT}$	Volumetric flowrate of heat carrier fluid entering the cold tank (m^3/s)
$V_{in,FC}$	Volumetric flowrate of heat carrier fluid leaving tank and entering fan coil (m^3/s)
$V_{in,HT}$	Volumetric flowrate of heat carrier fluid entering the hot tank (m^3/s)
$V_{in,IHX}$	Volumetric flowrate of heat carrier fluid through internal heat exchanger of tank (m^3/s)
$V_{in,IHX,CT}$	Volumetric flowrate of heat carrier fluid through internal heat exchanger of cold tank (m^3/s)
$V_{in,IHX,HT}$	Volumetric flowrate of heat carrier fluid through internal heat exchanger of hot tank (m^3/s)
$V_{out,CT}$	Volumetric flowrate of heat carrier fluid exiting the cold tank (m^3/s)

$V_{out,HT}$	Volumetric flowrate of heat carrier fluid exiting the hot tank (m^3/s)
V_{tank}	Tank volume (m^3)
$\%V_{glycol}$	Percentage by volume of glycol in heat carrier fluid (%)
Greek	
$\delta E_{Nh,CT,Exp}$	Measurement uncertainty of experimental energy losses during natural heat-up for cold tank (J)
$\delta E_{Nc,HT,Exp}$	Measurement uncertainty of experimental energy losses during natural cooldown for hot tank (J)
$\delta P_{Ch,CT,Exp}$	Measurement uncertainty of experimental charged power for cold tank (W)
$\delta P_{Ch,HT,Exp}$	Measurement uncertainty of experimental charged power for hot tank (W)
$\delta P_{Dis,CT,Exp}$	Measurement uncertainty of experimental discharged power for cold tank (W)
$\delta P_{Dis,HT,Exp}$	Measurement uncertainty of experimental discharged power for hot tank (W)
$\delta T_{in,CT}$	Measurement uncertainty of measured heat carrier fluid temperature at cold tank inlet (°C)
$\delta T_{in,HT}$	Measurement uncertainty of experimental heat carrier fluid temperature at hot tank inlet (°C)
$\delta T_{in,IHX,CT}$	Measurement uncertainty of experimental heat carrier fluid temperature at internal heat exchanger inlet of cold tank (°C)
$\delta T_{in,IHX,HT}$	Measurement uncertainty of experimental heat carrier fluid temperature at internal heat exchanger inlet of hot tank (°C)
$\delta T_{out,CT}$	Measurement uncertainty of experimental heat carrier fluid temperature at cold tank outlet (°C)
$\delta T_{out,HT}$	Measurement uncertainty of experimental heat carrier fluid temperature at hot tank outlet (°C)
$\delta T_{out,IHX,CT}$	Measurement uncertainty of experimental heat carrier fluid temperature at internal heat exchanger outlet of cold tank (°C)
$\delta T_{out,IHX,HT}$	Measurement uncertainty of experimental heat carrier fluid temperature at internal heat exchanger outlet of hot tank (°C)
$\delta \overline{T}_{CT,t_0}$	Measurement uncertainty of arithmetic average of experimental heat carrier fluid temperatures at four distinct heights inside cold tank at initial time t_0 (°C)
$\delta \overline{T}_{CT,t_f}$	Measurement uncertainty of arithmetic average of experimental heat carrier fluid temperatures at four distinct heights inside cold tank at initial time t_f (°C)
$\delta \overline{T}_{HT,t_0}$	Measurement uncertainty of arithmetic average of experimental heat carrier fluid temperatures at four distinct heights inside hot tank at initial time t_0 (°C)
$\delta \overline{T}_{HT,t_f}$	Measurement uncertainty of arithmetic average of experimental heat carrier fluid temperatures at four distinct heights inside hot tank at initial time t_f (°C)
$\delta V_{in,FC}$	Measurement uncertainty of measured volumetric flowrate exiting tank and entering fan coil (m^3/s)
$\delta V_{in,IHX,CT}$	Measurement uncertainty of measured volumetric flowrate at inlet of internal heat exchanger of cold tank (m^3/s)
$\delta V_{in,IHX,HT}$	Measurement uncertainty of measured volumetric flowrate at inlet of internal heat exchanger of hot tank (m^3/s)
ρ	Density of heat carrier fluid inside tank (kg/m^3)
$\Delta T_{Err,i}$	Difference between predicted and measured temperature (°C)

Appendix A

Table A1 reports the values of the AE and ABE (defined, respectively, using Equations (3) and (4)) for each of the six outputs associated with each of the 28 ANN models against the training database. The cells reporting the best and worst performances within each row are shaded, respectively, in green and red to facilitate the comparison.

Table A2 reports the values of the MSE and RMSE (defined, respectively, using Equations (5) and (6)) for each of the six outputs associated with each of the 28 ANN

models against the training database. The cells reporting the best and worst performances within each row are shaded, respectively, in green and red to facilitate the comparison.

Table A1. Average error and average absolute error for each of the 6 outputs associated with the 28 ANN models against the training database.

			AE·10^{-5} (°C)						ABE·10^{-3} (°C)					
	Neurons per Layer	Delay	T_{CT1}, T_{HT1}	T_{CT2}, T_{HT2}	T_{CT3}, T_{HT3}	T_{CT4}, T_{HT4}	$T_{out,IHX,CT}$, $T_{out,IHX,HT}$	$T_{out,CT}$, $T_{out,HT}$	T_{CT1}, T_{HT1}	T_{CT2}, T_{HT2}	T_{CT3}, T_{HT3}	T_{CT4}, T_{HT4}	$T_{out,IHX,CT}$, $T_{out,IHX,HT}$	$T_{out,CT}$, $T_{out,HT}$
ANN1	8	1	−9	−15	0	13	−1	4	8	7	10	8	12	8
ANN2	8	2	4	3	4	29	18	16	8	9	10	8	19	5
ANN3	8	4	56	62	51	−23	−149	44	11	9	11	10	23	7
ANN4	8	6	8	20	20	7	15	8	11	11	12	12	21	9
ANN5	12	1	−48	−38	−80	−67	−100	−64	6	6	10	5	17	5
ANN6	12	2	37	18	−54	185	290	−57	13	8	12	11	17	10
ANN7	12	4	6	−16	20	21	18	51	16	15	14	14	26	11
ANN8	12	6	31	55	29	28	10	24	16	13	14	15	23	13
ANN9	16	1	72	60	42	44	136	62	8	7	12	8	18	8
ANN 10	16	2	12	1	17	3	21	19	13	13	15	11	25	11
ANN 11	16	4	−466	−936	−307	−2227	−1548	−607	16	18	17	26	34	15
ANN 12	16	6	833	−715	−908	−2512	864	−1236	25	17	25	30	37	20
ANN 13	20	1	−299	−65	23	−88	−100	−138	10	10	13	9	24	9
ANN 14	20	2	−16	−17	−50	−15	−7	−19	11	13	14	12	22	9
ANN 15	20	4	43	37	39	47	5	41	12	13	15	16	26	11
ANN 16	20	6	352	237	344	467	481	103	14	14	15	14	27	13
ANN 17	24	1	−37	−44	−42	−10	−12	8	9	9	12	9	23	10
ANN 18	24	2	−83	−81	−101	−100	−72	−77	10	11	11	11	21	6
ANN 19	24	4	120	102	189	39	79	−13	12	12	14	11	23	9
ANN 20	24	6	1675	589	−1420	1639	213	232	28	21	23	26	37	17
ANN 21	28	1	−30	−38	−39	−53	−38	−47	8	7	8	8	21	5
ANN 22	28	2	45	17	50	8	−103	5	10	12	11	11	21	6
ANN 23	28	4	991	2260	3342	−603	1453	−35	20	34	40	24	41	16
ANN 24	28	6	−98	6	−28	61	−101	−47	12	12	12	13	21	6
ANN 25	32	1	407	489	88	464	5	466	11	12	13	11	25	12
ANN 26	32	2	−200	699	1498	−43	1513	675	24	16	23	19	32	16
ANN 27	32	4	518	−131	−130	129	182	14	32	28	23	24	41	23
ANN 28	32	6	−187	−137	−16	−161	−14	−221	13	15	13	13	22	8

Table A3 reports the values of the NRMSE and R^2 (defined, respectively, using Equations (7) and (8)) for each of the six outputs associated with each of the 28 ANN models against the training database. The cells reporting the best and worst performances within each row are shaded, respectively, in green and red to facilitate the comparison.

Table A4 reports the values of the AE, ABE, MSE, RMSE, NRMSE, and R^2 (defined by Equations (3)–(8)) upon varying the type of training experiment for the HT. The blank cells in this table correspond to the physically irrelevant measurements of each individual experiment. The green shading in this table has been given to the cells associated with the best performance for each line, while the red shading has been assigned to the worst performances.

Table A2. Mean square error and root mean square error for each of the 6 outputs associated with the 28 ANN models against the training database.

	Neurons per Layer	Delay	MSE·10^{-5} (°C^2)						RMSE·10^{-3} (°C)					
			T_{CT1}, T_{HT1}	T_{CT2}, T_{HT2}	T_{CT3}, T_{HT3}	T_{CT4}, T_{HT4}	$T_{out,IHX,CT}$, $T_{out,IHX,HT}$	$T_{out,CT}$, $T_{out,HT}$	T_{CT1}, T_{HT1}	T_{CT2}, T_{HT2}	T_{CT3}, T_{HT3}	T_{CT4}, T_{HT4}	$T_{out,IHX,CT}$, $T_{out,IHX,HT}$	$T_{out,CT}$, $T_{out,HT}$
ANN1	8	1	15	13	20	12	42	15	12	12	14	11	20	12
ANN2	8	2	18	21	45	13	133	7	13	15	21	12	36	8
ANN3	8	4	29	20	38	21	190	13	17	14	19	14	44	11
ANN4	8	6	32	97	47	55	776	34	18	31	22	23	88	18
ANN5	12	1	9	8	46	5	130	5	9	9	21	7	36	7
ANN6	12	2	130	26	40	25	148	47	36	16	20	16	38	22
ANN7	12	4	116	135	92	159	495	70	34	37	30	40	70	27
ANN8	12	6	300	80	264	166	298	469	55	28	51	41	55	68
ANN9	16	1	14	12	59	15	174	14	12	11	24	12	42	12
ANN 10	16	2	138	104	260	82	405	111	37	32	51	29	64	33
ANN 11	16	4	88	134	119	186	450	56	30	37	35	43	67	24
ANN 12	16	6	192	180	494	383	839	122	44	42	70	62	92	35
ANN 13	20	1	32	30	92	30	268	30	18	17	30	17	52	17
ANN 14	20	2	27	37	83	35	241	21	16	19	29	19	49	15
ANN 15	20	4	63	70	135	102	490	61	25	27	37	32	70	25
ANN 16	20	6	556	589	478	308	1612	251	75	77	69	55	127	50
ANN 17	24	1	23	23	69	20	301	25	15	15	26	14	55	16
ANN 18	24	2	20	26	70	28	253	7	14	16	26	17	50	9
ANN 19	24	4	128	68	102	120	233	46	36	26	32	35	48	22
ANN 20	24	6	463	255	273	268	756	220	68	51	52	52	87	47
ANN 21	28	1	14	11	59	13	241	7	12	10	24	11	49	8
ANN 22	28	2	29	111	221	55	273	7	17	33	47	23	52	8
ANN 23	28	4	281	575	392	579	876	571	53	76	63	76	94	76
ANN 24	28	6	71	183	184	299	358	52	27	43	43	55	60	23
ANN 25	32	1	44	52	91	46	296	50	21	23	30	21	54	22
ANN 26	32	2	112	127	412	138	342	246	33	36	64	37	58	50
ANN 27	32	4	324	213	209	302	706	344	57	46	46	55	84	59
ANN 28	32	6	165	328	462	438	617	344	41	57	68	66	79	59

Table A5 reports the values of the AE, ABE, MSE, RMSE, NRMSE, and R^2 (defined by Equations (3)–(8)) upon varying the type of training experiment for the CT. The blank cells in this table correspond to the physically irrelevant measurements of each individual experiment. The green shading in this table has been given to the cells associated with the best performance for each line, while the red shading has been assigned to the worst performances.

Table A6 describes both the eight independent training tests as well as the two independent verification tests in terms of total duration, sampling interval, number of samples per operating mode, and the starting and ending day/time.

Table A3. Normalized root mean square error and coefficient of determination R^2 for each of the 6 outputs associated with the 28 ANN models against the training database.

	Neurons per Layer	Delay	NRMSE·10^{-4}						R^2					
			T_{CT1}, T_{HT1}	T_{CT2}, T_{HT2}	T_{CT3}, T_{HT3}	T_{CT4}, T_{HT4}	$T_{out,IHX,CT}$, $T_{out,IHX,HT}$	$T_{out,CT}$, $T_{out,HT}$	T_{CT1}, T_{HT1}	T_{CT2}, T_{HT2}	T_{CT3}, T_{HT3}	T_{CT4}, T_{HT4}	$T_{out,IHX,CT}$, $T_{out,IHX,HT}$	$T_{out,CT}$, $T_{out,HT}$
ANN1	8	1	3	3	3	3	5	3	0.9999991	0.9999993	0.9999990	0.9999993	0.9999981	0.9999988
ANN2	8	2	3	3	5	3	8	2	0.9999990	0.9999989	0.9999977	0.9999992	0.9999940	0.9999995
ANN3	8	4	4	3	4	4	10	3	0.9999984	0.9999989	0.9999981	0.9999988	0.9999914	0.9999990
ANN4	8	6	4	7	5	6	19	5	0.9999982	0.9999949	0.9999977	0.9999967	0.9999650	0.9999973
ANN5	12	1	2	2	5	2	8	2	0.9999995	0.9999996	0.9999977	0.9999997	0.9999942	0.9999996
ANN6	12	2	9	4	5	4	8	5	0.9999927	0.9999987	0.9999980	0.9999985	0.9999933	0.9999963
ANN7	12	4	8	9	7	10	16	7	0.9999935	0.9999930	0.9999954	0.9999905	0.9999777	0.9999945
ANN8	12	6	13	7	12	10	12	17	0.9999832	0.9999958	0.9999869	0.9999901	0.9999866	0.9999632
ANN9	16	1	3	3	6	3	9	3	0.9999992	0.9999994	0.9999971	0.9999991	0.9999921	0.9999989
ANN 10	16	2	9	8	12	7	14	8	0.9999922	0.9999946	0.9999871	0.9999951	0.9999817	0.9999913
ANN 11	16	4	7	9	8	11	15	6	0.9999951	0.9999930	0.9999941	0.9999889	0.9999797	0.9999956
ANN 12	16	6	11	10	16	15	20	9	0.9999892	0.9999906	0.9999755	0.9999771	0.9999622	0.9999904
ANN 13	20	1	4	4	7	4	11	4	0.9999982	0.9999984	0.9999954	0.9999982	0.9999879	0.9999976
ANN 14	20	2	4	5	7	5	11	4	0.9999985	0.9999980	0.9999959	0.9999979	0.9999891	0.9999983
ANN 15	20	4	6	6	9	8	15	6	0.9999964	0.9999963	0.9999933	0.9999939	0.9999779	0.9999952
ANN 16	20	6	18	18	16	14	28	13	0.9999688	0.9999692	0.9999763	0.9999816	0.9999273	0.9999803
ANN 17	24	1	4	4	6	3	12	4	0.9999987	0.9999988	0.9999966	0.9999988	0.9999864	0.9999980
ANN 18	24	2	3	4	6	4	11	2	0.9999989	0.9999986	0.9999965	0.9999984	0.9999886	0.9999994
ANN 19	24	4	9	6	7	9	11	5	0.9999928	0.9999965	0.9999949	0.9999928	0.9999895	0.9999964
ANN 20	24	6	16	12	12	13	19	12	0.9999740	0.9999866	0.9999864	0.9999840	0.9999659	0.9999828
ANN 21	28	1	3	2	6	3	11	2	0.9999992	0.9999994	0.9999971	0.9999992	0.9999891	0.9999995
ANN 22	28	2	4	8	11	6	12	2	0.9999984	0.9999942	0.9999890	0.9999967	0.9999877	0.9999995
ANN 23	28	4	13	18	14	19	21	19	0.9999842	0.9999699	0.9999805	0.9999654	0.9999605	0.9999552
ANN 24	28	6	6	10	10	13	13	6	0.9999960	0.9999904	0.9999909	0.9999821	0.9999839	0.9999959
ANN 25	32	1	5	5	7	5	12	6	0.9999975	0.9999973	0.9999955	0.9999973	0.9999867	0.9999961
ANN 26	32	2	8	8	15	9	13	12	0.9999937	0.9999933	0.9999796	0.9999918	0.9999846	0.9999807
ANN 27	32	4	14	11	11	13	19	15	0.9999818	0.9999888	0.9999896	0.9999820	0.9999682	0.9999730
ANN 28	32	6	10	14	16	16	17	15	0.9999907	0.9999828	0.9999770	0.9999739	0.9999722	0.9999730

Table A4. Statistical metrics for the ANN5 configuration of the hot tank upon varying the training experiments.

Metrics	Parameter	Cooldown Test	Charging Test	Discharging Test	Simultaneous Discharging and Charging Test
AE·10^{-4} (°C)	T_{HT1}	−15	43	−64	4
	T_{HT2}	−22	52	−78	2
	T_{HT3}	−30	38	−53	−19
	T_{HT4}	−38	51	−72	8
	$T_{out,IHX,HT}$		41		−6
	$T_{out,HT}$			−58	−2
ABE·10^{-3} (°C)	T_{HT1}	6	6	7	5
	T_{HT2}	6	8	8	3
	T_{HT3}	5	11	7	29
	T_{HT4}	5	7	7	4
	$T_{out,IHX,HT}$		20		45
	$T_{out,HT}$			6	4

Table A4. *Cont.*

Metrics	Parameter	Cooldown Test	Charging Test	Discharging Test	Simultaneous Discharging and Charging Test
MSE·10^{-5} (°C^2)	T_{HT1}	5	14	14	4
	T_{HT2}	5	16	10	1
	T_{HT3}	4	197	10	122
	T_{HT4}	5	12	8	2
	$T_{out,IHX,HT}$		629		242
	$T_{out,HT}$			7	3
RMSE·10^{-3} (°C)	T_{HT1}	7	12	12	6
	T_{HT2}	7	13	10	4
	T_{HT3}	7	44	10	35
	T_{HT4}	7	11	9	5
	$T_{out,IHX,HT}$		79		49
	$T_{out,HT}$			8	6
NRMSE·10^{-4}	T_{HT1}	3	5	7	16
	T_{HT2}	3	5	6	10
	T_{HT3}	3	19	6	107
	T_{HT4}	3	5	5	10
	$T_{out,IHX,HT}$		30		220
	$T_{out,HT}$			5	13
R^2	T_{HT1}	0.9999986	0.9999948	0.9999926	0.9999058
	T_{HT2}	0.9999987	0.9999940	0.9999937	0.9999627
	T_{HT3}	0.9999989	0.9997075	0.9999938	0.9950490
	T_{HT4}	0.9999987	0.9999947	0.9999946	0.9999401
	$T_{out,IHX,HT}$		0.9976147		0.9900936
	$T_{out,HT}$			0.9999962	0.9999272

Table A5. Statistical metrics for the ANN5 configuration of the cold tank upon varying the training experiments.

Metrics	Parameter	Heat-Up Test	Charging Test	Discharging Test	Simultaneous Discharging and Charging Test
AE·10^{-4} (°C)	T_{CT1}	−6	−16	12	12
	T_{CT2}	−3	−12	55	−4
	T_{CT3}	1	−10	18	0
	T_{CT4}	−2	−13	50	−11
	$T_{out,IHX,CT}$		−16		6
	$T_{out,CT}$			13	10
ABE·10^{-3} (°C)	T_{CT1}	8	4	4	4
	T_{CT2}	7	4	6	7
	T_{CT3}	5	7	7	15
	T_{CT4}	5	3	5	2
	$T_{out,IHX,CT}$		12		21
	$T_{out,CT}$			3	3
MSE·10^{-5} (°C^2)	T_{CT1}	19	2	2	2
	T_{CT2}	12	3	5	8
	T_{CT3}	6	12	7	35
	T_{CT4}	5	2	7	1
	$T_{out,IHX,CT}$		38		71
	$T_{out,CT}$			3	2

Table A5. *Cont.*

Metrics	Parameter	Heat-Up Test	Charging Test	Discharging Test	Simultaneous Discharging and Charging Test
RMSE·10^{-3} (°C)	T_{CT1}	14	5	5	5
	T_{CT2}	11	6	7	9
	T_{CT3}	8	11	9	19
	T_{CT4}	7	4	8	3
	$T_{out,IHX,CT}$		19		27
	$T_{out,CT}$			5	4
NRMSE·10^{-4}	T_{CT1}	11	5	5	16
	T_{CT2}	11	6	7	25
	T_{CT3}	8	11	9	65
	T_{CT4}	8	4	8	11
	$T_{out,IHX,CT}$		34		112
	$T_{out,CT}$			5	13
R^2	T_{CT1}	0.9999857	0.9999943	0.9999963	0.9999033
	T_{CT2}	0.9999876	0.9999919	0.9999927	0.9997063
	T_{CT3}	0.9999924	0.9999724	0.9999890	0.9986572
	T_{CT4}	0.9999934	0.9999958	0.9999900	0.9999649
	$T_{out,IHX,CT}$		0.9994188		0.9981574
	$T_{out,CT}$			0.9999957	0.9999411

Table A6. Total duration, sampling interval, number of samples, starting/ending date/time of the independent training and verification databases.

	Test Description	Total Duration (min)	Sampling Interval (s)	Number of Samples	Starting Date- Time (dd/mm/yyyy)-(hh:mm:ss)	Ending Date- Time (dd/mm/yyyy)-(hh:mm:ss)
Four training tests for the HT	Natural cooldown experiment	7559.0	60	7560	13/04/2022- 11:43:35	18/04/2022- 17:28:27
	Charging experiment	403.0	5	4837	05/05/2022- 09:25:02	05/05/2022- 16:13:30
	Discharging experiment	312.0	5	3745	11/04/2022- 13:18:38	11/04/2022- 18:34:23
	Simultaneous discharging/charging experiment	337.0	5	4045	12/04/2022- 12:15:28	12/04/2022- 17:57:27
Four training tests for the CT	Natural heat-up experiment	7699.0	60	7700	09/05/2022- 18:24:08	15/05/2022- 02:43:38
	Charging experiment	529.5	5	6355	06/05/2022- 09:38:29	06/05/2022- 18:35:26
	Discharging experiment	233.0	5	2797	20/04/2022- 15:03:12	20/04/2022- 18:59:51
	Simultaneous discharging/charging experiment	331.0	5	3973	21/04/2022- 13:10:36	21/04/2022- 18:46:47
Verification test for the HT		540.0	5	6480	10/11/2022- 09:00:00	10/11/2022- 18:00:00
Verification test for the CT		540.0	5	6480	15/11/2022- 09:00:00	15/11/2022- 18:00:00

References

1. Dinçer, İ.; Rosen, M. *Thermal Energy Storage: Systems and Applications*, 3rd ed; John Wiley & Sons Ltd.: Hoboken, NJ, USA, 2021; pp. 1–653. [CrossRef]
2. Pinel, P.; Cruickshank, C.A.; Beausoleil-Morrison, I.; Wills, A. A Review of Available Methods for Seasonal Storage of Solar Thermal Energy in Residential Applications. *Renew. Sustain. Energy Rev.* **2011**, *15*, 3341–3359. [CrossRef]
3. Xu, J.; Wang, R.Z.; Li, Y. A Review of Available Technologies for Seasonal Thermal Energy Storage. *Sol. Energy* **2014**, *103*, 610–638. [CrossRef]
4. Ghalambaz, M.; Sheremet, M.; Fauzi, M.A.; Fteiti, M.; Younis, O. A Scientometrics Review of Solar Thermal Energy Storage (STES) during the Past Forty Years. *J. Energy Storage* **2023**, *66*, 107266. [CrossRef]
5. Ciampi, G.; Ciervo, A.; Rosato, A.; Sibilio, S.; Di Nardo, A. Parametric Simulation Analysis of a Centralized Solar Heating System with Long-Term Thermal Energy Storage Serving a District of Residential and School Buildings in Italy. *Adv. Model. Anal. A* **2018**, *55*, 165–172. [CrossRef]

6. Scapino, L.; Zondag, H.A.; Diriken, J.; Rindt, C.C.M.; Van Bael, J.; Sciacovelli, A. Modeling the Performance of a Sorption Thermal Energy Storage Reactor Using Artificial Neural Networks. *Appl. Energy* **2019**, *253*, 113525. [CrossRef]
7. Lamrani, B.; Alqahtani, R.T.; Ajbar, A.; Benaicha, M. Dynamic Performance Analysis of Sensible and Latent Cold Thermal Energy Storage Systems for Building Cooling Networks. *Case Stud. Therm. Eng.* **2025**, *71*, 106264. [CrossRef]
8. Elsheikh, A.H.; Sharshir, S.W.; Abd Elaziz, M.; Kabeel, A.E.; Guilan, W.; Haiou, Z. Modeling of Solar Energy Systems Using Artificial Neural Network: A Comprehensive Review. *Sol. Energy* **2019**, *180*, 622–639. [CrossRef]
9. Ji, H.Y.; Kang, C.; Park, D. Experiment and Prediction Analysis of Thermal Energy Storage for Heat Load Balancing in Domestic Hot Water System. *Energy* **2024**, *313*, 134040. [CrossRef]
10. American Society of Heating, Refrigerating and Air-Conditioning Engineers (ASHRAE). *2017 ASHRAE Handbook—Fundamentals*, SI ed.; American Society of Heating, Refrigerating and Air-Conditioning Engineers, Inc.: Atlanta, GA, USA, 2017.
11. Géczy-Víg, P.; Farkas, I. Neural Network Modelling of Thermal Stratification in a Solar DHW Storage. *Sol. Energy* **2010**, *84*, 801–806. [CrossRef]
12. Yaïci, W.; Entchev, E. Performance Prediction of a Solar Thermal Energy System Using Artificial Neural Networks. *Appl. Therm. Eng.* **2014**, *73*, 1348–1359. [CrossRef]
13. Kalogirou, S.A. Applications of Artificial Neural-Networks for Energy Systems. *Appl. Energy* **2000**, *67*, 17–35. [CrossRef]
14. Rojas Cala, E.F.; Béjar, R.; Mateu, C.; Borri, E.; Romagnoli, A.; Cabeza, L.F. Modeling of TES Tanks by Means of CFD Simulation Using Neural Networks. *Energies* **2025**, *18*, 511. [CrossRef]
15. Soomro, A.A.; Mokhtar, A.A.; Akbar, A.; Abbasi, A. Modelling Techniques Used in the Analysis of Stratified Thermal Energy Storage: A Review. *MATEC Web Conf.* **2018**, *225*, 01015. [CrossRef]
16. Sioshansi, R.; Denholm, P.; Arteaga, J.; Awara, S.; Bhattacharjee, S.; Botterud, A.; Cole, W.; Cortes, A.; De Queiroz, A.; Decarolis, J.; et al. Energy-Storage Modeling: State-of-the-Art and Future Research Directions. *IEEE Trans. Power Syst.* **2022**, *37*, 860–875. [CrossRef]
17. Amarasinghe, K.; Wijayasekara, D.; Carey, H.; Manic, M.; He, D.; Chen, W.P. Artificial Neural Networks Based Thermal Energy Storage Control for Buildings. In *IECON 2015—41st Annual Conference of the IEEE Industrial Electronics Society*; IEEE: Yokohama, Japan, 2015; pp. 5421–5426. [CrossRef]
18. Lee, D.; Ooka, R.; Ikeda, S.; Choi, W. Artificial Neural Network Prediction Models of Stratified Thermal Energy Storage System and Borehole Heat Exchanger for Model Predictive Control. *Sci. Technol. Built Environ.* **2019**, *25*, 534–548. [CrossRef]
19. MATLAB, MathWorks. Available online: https://www.mathworks.com/products/matlab.html (accessed on 9 December 2025).
20. Ameri Siahoui, H.R.; Dehghani, A.R.; Razavi, M.; Khani, M.R. Investigation of Thermal Stratification in Cisterns Using Analytical and Artificial Neural Networks Methods. *Energy Convers. Manag.* **2011**, *52*, 505–511. [CrossRef]
21. Diez, F.J.; Navas, L.M.; Martínez, A. Prediction and Identification of the Evolution of Solar-Heated Hot Water Temperature in a Stratified Tank in Static Mode Using Artificial Neural Networks. *Appl. Sol. Energy* **2016**, *52*, 183–192. [CrossRef]
22. Géczy-Víg, P.; Farkas, I. Influence of the Time Step in Ann Modelling of Thermal Stratification of Solar Storage. In Proceedings of the IFAC Proceedings Volumes (IFAC-PapersOnline), Seoul, Republic of Korea, 6–11 July 2008; Volume 41.
23. Kalogirou, S.A.; Panteliou, S.; Dentsoras, A. Modeling of Solar Domestic Water Heating Systems Using Artificial Neural Networks. *Sol. Energy* **1999**, *65*, 335–342. [CrossRef]
24. Souliotis, M.; Kalogirou, S.; Tripanagnostopoulos, Y. Modelling of an ICS Solar Water Heater Using Artificial Neural Networks and TRNSYS. *Renew. Energy* **2009**, *34*, 1333–1339. [CrossRef]
25. TRNSYS—Transient System Simulation Tool. Available online: http://www.trnsys.com (accessed on 9 December 2025).
26. Wang, Y.; Chen, J.; Cao, B.; Liu, X.; Zhang, X. Energy Consumption Prediction of Cold Storage Based on LSTM with Parameter Optimization. *Int. J. Refrig.* **2025**, *175*, 12–24. [CrossRef]
27. Cheng, J.; Jin, S.; Zheng, Z.; Hu, K.; Yin, L.; Wang, Y. Energy Consumption Prediction for Water-Based Thermal Energy Storage Systems Using an Attention-Based TCN-LSTM Model. *Sustain. Cities Soc.* **2025**, *126*, 106383. [CrossRef]
28. Saikia, P.; Bastida, H.; Ugalde-Loo, C.E. An Effective Predictor of the Dynamic Operation of Latent Heat Thermal Energy Storage Units Based on a Non-Linear Autoregressive Network with Exogenous Inputs. *Appl. Energy* **2024**, *360*, 122697. [CrossRef]
29. Badji, A.; Benseddik, A.; Bensaha, H.; Boukhelifa, A.; Bouhoun, S.; Nettari, C.; Kherrafi, M.A.; Lalmi, D. Experimental Assessment of a Greenhouse with and without PCM Thermal Storage Energy and Prediction Their Thermal Behavior Using Machine Learning Algorithms. *J. Energy Storage* **2023**, *71*, 108133. [CrossRef]
30. Billings, S.A. *Nonlinear System Identification: NARMAX Methods in the Time, Frequency, and Spatio-Temporal Domains*; John Wiley & Sons, Ltd.: Hoboken, NJ, USA, 2013; pp. 1–555. [CrossRef]
31. Karim, F.; Majumdar, S.; Darabi, H.; Chen, S. LSTM Fully Convolutional Networks for Time Series Classification. *IEEE Access* **2017**, *6*, 1662–1669. [CrossRef]
32. Kratzert, F.; Klotz, D.; Brenner, C.; Schulz, K.; Herrnegger, M. Rainfall-Runoff Modelling Using Long Short-Term Memory (LSTM) Networks. *Hydrol. Earth Syst. Sci.* **2018**, *22*, 6005–6022. [CrossRef]

33. Rosato, A.; El Youssef, M.; Daoud, H.; Al-Salaymeh, A.; Ghorab, M.G. TRNSYS Dynamic Digital Twin of Hot and Cold Sensible Thermal Energy Storages: An Experimental Calibration and Validation Approach. *J. Energy Storage* **2025**, *105*, 114700. [CrossRef]
34. Rosato, A.; Guarino, F.; Filomena, V.; Sibilio, S.; Maffei, L. Experimental Calibration and Validation of a Simulation Model for Fault Detection of HVAC Systems and Application to a Case Study. *Energies* **2020**, *13*, 3948. [CrossRef]
35. Heizer. Model Zani PUIW-3. Available online: https://zani.it/pdf/PU_PUW_PIUW.pdf (accessed on 9 December 2025).
36. Rhoss S.p.A. YARDY EV3 Fan Coil. Available online: https://doming.rs/cms_upload/catalog/product_files/2070127_fan_coils_yardy_ev3.pdf (accessed on 9 December 2025).
37. E + E Elektronik. EE210 Outdoor Temperature and Relative Humidity Sensor. Available online: https://www.epluse.com/fileadmin/data/product/ee210/datasheet_EE210_Outdoor.pdf (accessed on 9 December 2025).
38. TSI Incorporated. Q-Trak™ Multi-Function Indoor Air Quality Monitor. Available online: https://tsi.com/getmedia/d2a8d1d1-7551-47fe-8a0f-3c14b09b494b/7575_QTrak_A4_UK_5001356-web?ext=.pdf (accessed on 9 December 2025).
39. Endress + Hauser. Proline Promag E 100 Electromagnetic Flowmeter. Available online: https://bdih-download.endress.com/file/005056A5E3831EDBB8DDE7F962CC913F/TI01159DEN_0317.pdf (accessed on 9 December 2025).
40. Metron S.p.A. PT 100 Heat Carrier Fluid Temperature Sensor. Available online: https://shop.measureit.eu/sensori.html (accessed on 9 December 2025).
41. BELIMO Italia S.r.l. EV020R + BAC Energy Valve Volume Percentage of Glycol Sensor. Available online: https://www.belimoseoul.com/data/medium/9d020b80b518dcf144d3cc8db59f777e.pdf (accessed on 9 December 2025).
42. Angrisani, G.; Canelli, M.; Roselli, C.; Sasso, M. Calibration and Validation of a Thermal Energy Storage Model: Influence on Simulation Results. *Appl. Therm. Eng.* **2014**, *67*, 190–200. [CrossRef]
43. Nash, A.L.; Badithela, A.; Jain, N. Dynamic Modeling of a Sensible Thermal Energy Storage Tank with an Immersed Coil Heat Exchanger under Three Operation Modes. *Appl. Energy* **2017**, *195*, 877–889. [CrossRef]
44. Soomro, A.A.; Mokhtar, A.A.; Salilew, W.M.; Abdul Karim, Z.A.; Abbasi, A.; Lashari, N.; Jameel, S.M. Machine Learning Approach to Predict the Performance of a Stratified Thermal Energy Storage Tank at a District Cooling Plant Using Sensor Data. *Sensors* **2022**, *22*, 7687. [CrossRef] [PubMed]
45. ASHRAE. Chapter 21: Physical Properties of Secondary Coolants (Brines). In *Handbook-Chapter, ASHRAE Fundamentals*; American Society of Heating, Refrigerating and Air-Conditioning Engineers, Inc.: Atlanta, GA, USA, 2005.
46. Moffat, R.J. Using Uncertainty Analysis in the Planning of an Experiment. *ASME J. Fluids Eng.* **1985**, *1072*, 173–178. [CrossRef]
47. Mastrullo, R.; Rosato, A.; Vanoli, G.P.; Thome, J.R. A Methodology to Select the Experimental Plant Instrumentation Based on an a Priori Analysis of Measurement Errors and Instrumentation Cost. *Int. Commun. Heat Mass Transf.* **2008**, *35*, 689–695. [CrossRef]
48. Rosato, A.; Guarino, F.; El Youssef, M.; Capozzoli, A.; Masullo, M.; Maffei, L. Faulty Operation of Coils' and Humidifier Valves in a Typical Air-Handling Unit: Experimental Impact Assessment of Indoor Comfort and Patterns of Operating Parameters under Mediterranean Climatic Conditions. *Energies* **2022**, *15*, 6781. [CrossRef]
49. Rosato, A.; El Youssef, M.; Guarino, F.; Ciervo, A.; Sibilio, S. Experimental Studies of Air-Handling Units' Faulty Operation for the Development of Data-Driven Fault Detection and Diagnosis Tools: A Systematic Review. *Energy Rep.* **2022**, *8*, 494–503. [CrossRef]
50. Rosato, A.; Guarino, F.; El Youssef, M.; Capozzoli, A.; Masullo, M.; Maffei, L. Experimental Assessment of Ground-Truth Faults in a Typical Single-Duct Dual-Fan Air-Handling Unit under Mediterranean Climatic Conditions: Impact Scenarios of Sensors' Offset and Fans' Failure. *Energy Build.* **2022**, *275*, 112492. [CrossRef]
51. van Schalkwyk, P.D.; Meyer, J.P.; Engelbrecht, J.A.A.; Booysen, M.J. Numerical Modelling of Thermal Stratification Scenarios in Horizontal Electric Hot Water Storage Tanks. *Appl. Therm. Eng.* **2025**, *258*, 124716. [CrossRef]
52. Zhang, T.; Strbac, G. Artificial Intelligence Applications for Energy Storage: A Comprehensive Review. *Energies* **2025**, *18*, 4718. [CrossRef]

Disclaimer/Publisher's Note: The statements, opinions and data contained in all publications are solely those of the individual author(s) and contributor(s) and not of MDPI and/or the editor(s). MDPI and/or the editor(s) disclaim responsibility for any injury to people or property resulting from any ideas, methods, instructions or products referred to in the content.